

# Diagrammatic Tools for Generating Biorthogonal Multiresolutions

Faramarz F. Samavati  
Computer Science Department  
University of Calgary  
Calgary, Alberta T2N 1N4  
Canada  
samavati@cpsc.ucalgary.ca

Richard H. Bartels  
Computer Graphics Laboratory  
Computer Science Department  
University of Waterloo  
Waterloo, Ontario N2L 3G1  
Canada  
rhhbartel@cgl.uwaterloo.ca

April 26, 2003

## Abstract

In a previous work [1] we introduced a construction designed to produce biorthogonal multiresolutions from given subdivisions. This construction was formulated in matrix terms, which is appropriate for curves and tensor-product surfaces. For mesh surfaces of non-tensor connectivity, however, matrix notation is inconvenient. This work introduces diagrams and diagram interactions to replace matrices and matrix multiplication. The diagrams we use are patterns of value-labeled nodes, one type of diagram corresponding to each row or column of one of the matrices of a biorthogonal system. All types of diagrams used in the construction are defined on a common mesh of the multiresolution.

**keywords:** subdivision, triangle meshes, least squares, biorthogonal, multiresolution.

## 1 Introduction

The material developed in [1] proposed a local, least squares construction for processing geometric data into a multiresolution form. The construction starts by selecting an existing subdivision algorithm applicable to the data and ends with a multiresolution that yields decomposition and reconstruction filters with only a finite number of nonzero elements in each filter. These filters depend upon the selected subdivision and upon the extent of locality chosen for the least squares approximation.

We begin in Section 2 by summarizing the construction. Section 3 introduces some terminology that helps us to position our diagrams on  $c^{k+1}$  meshes. Section 4 introduces some diagrams and diagram interactions as a replacement for matrices and matrix multiplication in the context of curve meshes.

*Stencils* and *masks* have long been used as tools to describe mesh subdivision; e.g. in [7]. We are adapting and modifying these tools here for the purposes of our construction steps; the relationship between our diagrams and those pre-existing tools will be evident to readers familiar with those tools. Any adjustments that have been made are to enable our diagrams to mimic the row/column-product properties of the decomposition and reconstruction matrices that are needed for our construction, which is not an issue primarily addressed by conventional masks and stencils.

Section 2, Section 3, and Section 4 are not intended to re-visit the merits of our construction of multiresolutions or any of its open problems; these sections merely serve to reformulate the construction in diagrammatic terms. Section 5 employs the diagrams to illustrate the construction at the boundary of a curve mesh.

Section 6 carries our diagrams over to surfaces, specifically to triangular surface meshes. This section establishes the conventions for using diagrams on such meshes.

To handle a potential explosion of bilinear equations in the case of surfaces, the construction of [1] is modified slightly by means of an appeal to the process of lifting [10]. This is covered in Section 7.

We use Butterfly subdivision [2, 12], which is interpolatory, and a subdivision by Litke, et. al., [6], which is not interpolatory, as examples. The diagrammatic representation of a multiresolution for Butterfly subdivision is given in Section 8 and that for the subdivision of Litke, et. al., is given in Section 9. It is hoped that the description of how triangular surfaces can be handled will be clear enough to enable the reader to adapt the diagrammatic approach to surface meshes of other regular connectivities (although subdivision rules for regular connectivities other than triangular are not often found in the literature).

In Section 10 we give an indication that the material on constructing multiresolutions at the boundaries of curves in Section 5 carries over to surfaces.

We close with a few examples in Section 11.

## 2 Review of Construction

A subdivision may be expressed in matrix form as

$$\mathbf{c}^{k+1} = \mathbf{P}\mathbf{c}^k \tag{2.1}$$

whereby a “coarse mesh,” whose points are arranged in the vector  $\mathbf{c}^k$ , is converted into a larger “fine mesh” of points, arranged in the vector  $\mathbf{c}^{k+1}$ , by the “subdivision matrix”  $\mathbf{P}$ . Nowhere in this matrix-vector notation is there any information about the mesh’s edge connectivity joining the points of  $\mathbf{c}^k$  or the points of  $\mathbf{c}^{k+1}$ . Hence, (2.1) can just as easily express the subdivision of surfaces as it can of curves, at least in terms of the conversion of coarse points to fine ones. This offers the advantage of a set of uniform mathematical tools with which to study subdivision, but it has the disadvantage of requiring important mesh information to be carried along separately. A useful byproduct of our work here is that, by formulating our construction in diagrammatic terms, we re-associate this connectivity information with the mathematical operations.

The construction is more interesting, and more practically useful, if the vector of points  $\mathbf{c}^{k+1}$  does not result from a subdivision; that is,  $\mathbf{c}^{k+1} \neq \mathbf{P}\mathbf{c}^k$  for any vector of points  $\mathbf{c}^k$ . In this case we wish to find a vector  $\mathbf{c}^k$  so that  $\mathbf{c}^{k+1} \approx \hat{\mathbf{c}}^{k+1} \equiv \mathbf{P}\mathbf{c}^k$ , so that the residuals  $\mathbf{c}^{k+1} - \hat{\mathbf{c}}^{k+1}$  are small, and so that complete information about these residuals can be stored in the space used for  $\{c^{k+1}\} \setminus \{c^k\}$  (or one of an equivalent size). Informally, this describes the features of a biorthogonal multiresolution built upon  $\mathbf{P}$ , which is the goal of the construction.

We begin with meshes for curves; that is, sets for which the mesh connectivity of the points  $\{c^k\}$ , and also for  $\{c^{k+1}\}$ , is simply that of a linear sequence. Subdivision matrices for these simple meshes are banded, repetitive, and slanted. That is; each column  $j$  of  $\mathbf{P}$  has only a finite number of nonzero entries, located from some row  $r_j$  through a lower row  $r_j + \ell$ ; these nonzero numbers appear in all columns save for a few exceptions (corresponding to the boundaries of the curve  $\{c^k\}$ ), and the entries of each succeeding

or preceding column are shifted down or up by some fixed number of rows (which number is determined by the *dilation scale* of the nested function spaces underlying the subdivision).

$$\mathbf{P} = \begin{bmatrix} \frac{1}{2} & \frac{1}{2} & 0 & 0 & 0 \\ \frac{1}{8} & \frac{3}{4} & \frac{1}{8} & 0 & 0 \\ 0 & \frac{1}{2} & \frac{1}{2} & 0 & 0 \\ 0 & \frac{1}{8} & \frac{3}{4} & \frac{1}{8} & 0 \\ 0 & 0 & \frac{1}{2} & \frac{1}{2} & 0 \\ 0 & 0 & \frac{1}{8} & \frac{3}{4} & \frac{1}{8} \\ 0 & 0 & 0 & \frac{1}{2} & \frac{1}{2} \end{bmatrix} \begin{matrix} c_{i-1}^{k+1} \\ c_i^{k+1} \\ c_{i+1}^{k+1} \\ \\ \\ \\ c_{j-1}^k \quad c_j^k \quad c_{j+1}^k \end{matrix} \quad (2.2)$$

To have a concrete example for illustration, we take the subdivision provided by midpoint knot insertion for uniform cubic B-splines (which provides a 2-scale dilation for a nesting of uniform-knot spline spaces). A finite (7-row, 5-column) portion of the interior of the  $\mathbf{P}$  matrix for this subdivision is given as (2.2).

A biorthogonal multiresolution based upon  $\mathbf{P}$  consists of the matrix  $\mathbf{P}$  together with matrices  $\mathbf{A}$ ,  $\mathbf{B}$ , and  $\mathbf{Q}$  that satisfy

$$\begin{aligned} \mathbf{AP} &= \mathbf{I} \\ \mathbf{BP} &= \mathbf{O} \\ \mathbf{AQ} &= \mathbf{O} \\ \mathbf{BQ} &= \mathbf{I} \end{aligned} \quad (2.3)$$

This system is a multiresolution in the sense that, if  $\mathbf{c}^{k+1}$  is the vector formed from a given sequence of points  $\{c^{k+1}\}$ , not necessarily produced by (2.1), and if the vector  $\mathbf{c}^k$  is defined by

$$\mathbf{c}^k = \mathbf{Ac}^{k+1} \quad (2.4)$$

and if the vector  $\mathbf{d}^k$  is defined by

$$\mathbf{d}^k = \mathbf{Bc}^{k+1} \quad (2.5)$$

then the sequence  $\{c^{k+1}\}$  can be recovered from the vector  $\mathbf{c}^{k+1}$  using  $\mathbf{c}^k$  and  $\mathbf{d}^k$  in a subdivision plus a correction:

$$\mathbf{c}^{k+1} = \mathbf{Pc}^k + \mathbf{Qd}^k \quad (2.6)$$

The construction of [1] is directed toward finding examples of  $\mathbf{A}$ ,  $\mathbf{B}$ , and  $\mathbf{Q}$  that are also banded, repetitive, and slanted; specifically, that have these characteristics for the columns of  $\mathbf{Q}$  and for the rows of  $\mathbf{A}$  and  $\mathbf{B}$ . Examples corresponding to (2.2) will be shown in (2.12), (2.13), and (2.14) below.

The construction is staged as follows:

1. a matrix  $\mathbf{A}$  is produced that satisfies the first matrix equation of (2.3);

2. trial versions of  $\mathbf{B}$  and  $\mathbf{Q}$  are produced, containing partially constrained symbolic entries, that satisfy the second and third matrix equations of (2.3);
3. the fourth matrix equation of (2.3) is solved to fix  $\mathbf{B}$  and  $\mathbf{Q}$ .

In each stage, advantage is taken of the fact that the matrices are banded, repetitive, and slanted. This means that any scalar equation that forms a part of the matrix equation in (2.3) is entirely characterized by the interaction of a row of the left-hand matrix with only one of a small number of adjacent columns of the right-hand matrix. (Alternatively, the scalar equations can be studied by looking at the interaction of a column of the right-hand matrix with only a small number of adjacent rows in the left-hand matrix.) The repetitiveness offers us the benefit of being able to characterize the entire matrix-matrix product (or at least, all of it except for a few special cases at the boundary) by studying how one representative row (or column) interacts with a small number of columns (rows).

This construction, and the multiresolution that results, is based upon the following premises:

- I. The fine mesh  $\{c^{k+1}\}$  consists of geometric points;
- II. The goal is to produce a coarse mesh  $\{c^k\}$ , where each coarse point is approximated by the fine points within a chosen neighborhood in a geometrically reasonable way;
- III. The approximated coarse points, when subdivided:  $\mathbf{P}c^k = \hat{c}^{k+1}$ , will return the fine mesh with small, Euclidian-distance errors  $c_i^{k+1} - \hat{c}_i^{k+1}$ ;
- IV. The errors are to be represented by quantities  $\{d^k\}$  in such a way that
  - (a)  $\{c^k\} \cup \{d^k\}$  will require the same storage space as  $\{c^{k+1}\}$ ;
  - (b) The magnitude of each  $d_\ell^k$  will be comparable to the magnitude of the distance errors in an easily determinable neighborhood.

The construction is, of course, carried out only once for each choice of regular subdivision and connectivity. The rows of  $\mathbf{A}$ ,  $\mathbf{B}$ ,  $\mathbf{P}$ , and  $\mathbf{Q}$  are treated as *filters* to be applied to points and difference information to *decompose* the fine mesh as in (2.4) and (2.5):

$$c_j^k = \sum_{\lambda} a_{\lambda} c_{\lambda}^{k+1} \quad (2.7)$$

$$d_{\ell}^k = \sum_{\mu} b_{\mu} c_{\mu}^{k+1} \quad (2.8)$$

and to *reconstruct* it as in (2.6):

$$c_i^{k+1} = \sum_{\rho} p_{\rho} c_{\rho}^k + \sum_{\sigma} q_{\sigma} d_{\sigma}^k \quad (2.9)$$

The filters may be applied simply and quickly to any new mesh that is encountered, provided its connectivity is appropriate for the subdivision under consideration.

As an example, the following illustrates the complete setup of equations to specify the elements of any general, interior row of  $\mathbf{A}$  for cubic B-spline subdivision under the assumption that there are 7 nonzero

elements in the row, and that in the row defining the value of  $c_j^k$  they are centered on the position corresponding to  $c_i^{k+1}$ :

$$\begin{bmatrix} a_{i-3} & a_{i-2} & a_{i-1} & a_i & a_{i+1} & a_{i+2} & a_{i+3} \end{bmatrix} \begin{bmatrix} \frac{1}{2} & \frac{1}{2} & 0 & 0 & 0 \\ \frac{1}{8} & \frac{3}{4} & \frac{1}{8} & 0 & 0 \\ 0 & \frac{1}{2} & \frac{1}{2} & 0 & 0 \\ 0 & \frac{1}{8} & \frac{3}{4} & \frac{1}{8} & 0 \\ 0 & 0 & \frac{1}{2} & \frac{1}{2} & 0 \\ 0 & 0 & \frac{1}{8} & \frac{3}{4} & \frac{1}{8} \\ 0 & 0 & 0 & \frac{1}{2} & \frac{1}{2} \end{bmatrix} = [0 \ 0 \ 1 \ 0 \ 0] \quad (2.10)$$

These are the only nontrivial scalar equations obtainable from the interior rows of  $\mathbf{A}$  and interior columns of  $\mathbf{P}$ , assuming this width and positioning for the elements in each row of  $\mathbf{A}$ . The interaction of this row of  $\mathbf{A}$  with any other interior column of  $\mathbf{P}$  involves only sums of products with one factor in each product equal to zero. Interactions coming from the boundary will produce a small number of scalar equations distinct from the ones in (2.10). These distinct equations have no effect on the ones shown in (2.10). They will be solved separately to yield  $\mathbf{A}$  values that are to be applied only to specific points at the boundary. An example of this will be given in Section 5.

By solving the equations represented by (2.10) for the  $\mathbf{A}$  elements of minimum Euclidian norm:

$$\left[ \begin{array}{cccccc} \frac{23}{196} & -\frac{23}{49} & \frac{9}{28} & \frac{52}{49} & \frac{9}{28} & -\frac{23}{49} & \frac{23}{196} \end{array} \right] \quad (2.11)$$

the point  $c_j^k = a_{i-3}c_{i-3}^{k+1} + \dots + a_{i+3}c_{i+3}^{k+1}$  represents a local least squares estimate based upon the 7 consecutive fine points  $c_{i-3}^{k+1}, \dots, c_{i+3}^{k+1}$  [1]. Figure 1 will illustrate that these 7 consecutive fine points are those that are physically nearest to and symmetrically placed about  $c_j^k$ . This is arguably the configuration of choice for estimating  $c_j^k$  in a least squares sense from a local neighborhood of points  $c_i^{k+1}$ , and it is in this sense, I. through III. above are addressed. With the same motivation, 1, 3, 5, 9, or more consecutive points  $c_{i\pm\lambda}^{k+1}$  could be chosen for the estimate, producing other options for  $\mathbf{A}$ , and then correspondingly for  $\mathbf{B}$  and  $\mathbf{Q}$ . (The restriction to estimates based upon odd numbers of points comes from the wish to approximate  $c_j^k$  by fine points  $c^{k+1}$  that range symmetrically about the probable mesh location of this coarse point.)

To handle the second matrix equation of (2.3), scalar equations corresponding to the nontrivial interactions of one row of  $\mathbf{B}$  with the columns of  $\mathbf{P}$  are set up in a similar way, assuming a number of nonzeros in a row of  $\mathbf{B}$  and a position for those nonzeros in the row defining the generic element  $d_\lambda^k$ . These scalar equations (along with any additional ones desired to enforce, for example, symmetry in the values of the row elements) are solved using a symbolic algebra system. Enough elements should be assumed in a row of  $\mathbf{B}$  so that the solution is not fully defined and has free variables.

To handle the third matrix equation of (2.3), scalar equations corresponding to the nontrivial interactions of one column of  $\mathbf{Q}$  with the rows of  $\mathbf{A}$  are set up in a similar way, with assumptions about number and position of nonzeros being made. Additional conditions of symmetry are also possible. The equations are solved in symbolic algebra, and the result must also contain free variables.

The final matrix equation of (2.3) is handled by using the symbolic results of the preceding two steps to generate the scalar equations representing the nontrivial interactions of a single row of  $\mathbf{B}$  with the

columns of  $\mathbf{Q}$  (or a single column of  $\mathbf{Q}$  with the rows of  $\mathbf{B}$ ), and the resulting (bilinear) equations are solved. Any remaining free variables may be fixed at will (our preference being to establish a norm of approximately unity for any column of  $\mathbf{Q}$ ).

A consistent set of solutions for cubic B-spline subdivision yields  $\mathbf{A}$  as follows (a  $5 \times 7$  slice):

$$\begin{bmatrix} \frac{9}{28} & -\frac{23}{49} & \frac{23}{196} & 0 & 0 & 0 & 0 \\ \frac{9}{28} & \frac{52}{49} & \frac{9}{28} & -\frac{23}{49} & \frac{23}{196} & 0 & 0 \\ \frac{23}{196} & -\frac{23}{49} & \frac{9}{28} & \frac{52}{49} & \frac{9}{28} & -\frac{23}{49} & \frac{23}{196} \\ 0 & 0 & \frac{23}{196} & -\frac{23}{49} & \frac{9}{28} & \frac{52}{49} & \frac{9}{28} \\ 0 & 0 & 0 & 0 & \frac{23}{196} & -\frac{23}{49} & \frac{9}{28} \end{bmatrix} \begin{matrix} c_{j-1}^k \\ c_j^k \\ c_{j+1}^k \\ c_{i-1}^{k+1} \\ c_i^{k+1} \\ c_{i+1}^{k+1} \end{matrix} \quad (2.12)$$

A corresponding ( $5 \times 7$ ) slice of one possible  $\mathbf{B}$  matrix is:

$$\begin{bmatrix} \frac{39}{49} & -\frac{26}{49} & \frac{13}{98} & 0 & 0 & 0 & 0 \\ \frac{13}{98} & -\frac{26}{49} & \frac{39}{49} & -\frac{26}{49} & \frac{13}{98} & 0 & 0 \\ 0 & 0 & \frac{13}{98} & -\frac{26}{49} & \frac{39}{49} & -\frac{26}{49} & \frac{13}{98} \\ 0 & 0 & 0 & 0 & \frac{13}{98} & -\frac{26}{49} & \frac{39}{49} \\ 0 & 0 & 0 & 0 & 0 & 0 & \frac{13}{98} \end{bmatrix} \begin{matrix} d_{\ell-1}^k \\ d_{\ell}^k \\ d_{\ell+1}^k \\ c_{i-1}^{k+1} \\ c_i^{k+1} \\ c_{i+1}^{k+1} \end{matrix} \quad (2.13)$$

And a corresponding ( $7 \times 5$ ) portion of a possible  $\mathbf{Q}$  matrix is:

$$\begin{bmatrix} 1 & -\frac{23}{52} & 0 & 0 & 0 \\ -\frac{63}{208} & -\frac{63}{208} & -\frac{23}{208} & 0 & 0 \\ -\frac{23}{52} & 1 & -\frac{23}{52} & 0 & 0 \\ -\frac{23}{208} & -\frac{63}{208} & -\frac{63}{208} & -\frac{23}{208} & 0 \\ 0 & -\frac{23}{52} & 1 & -\frac{23}{52} & 0 \\ 0 & -\frac{23}{208} & -\frac{63}{208} & -\frac{63}{208} & -\frac{23}{208} \\ 0 & 0 & -\frac{23}{52} & 1 & -\frac{23}{52} \end{bmatrix} \begin{matrix} c_{i-1}^{k+1} \\ c_i^{k+1} \\ c_{i+1}^{k+1} \\ d_{\ell-1}^k \\ d_{\ell}^k \\ d_{\ell+1}^k \end{matrix} \quad (2.14)$$

Observations and considerations of the following nature address IV. (a) and (b): The construction of  $\mathbf{B}$  and  $\mathbf{Q}$  ends with the selection of left over free parameters, and it is our custom to use these so that

the maximum magnitude element (the infinity vector norm) of each column of  $\mathbf{Q}$  is comparable to 1 in magnitude, expecting that this means the contribution of each  $d_\ell^k$  in any residual will be comparable to the magnitude of  $d_\ell^k$  itself. The residuals  $c_i^{k+1} - c_i^{k+1}$  to which  $d_\ell^k$  contributes are those corresponding to the nonzero elements of the  $\ell^{\text{th}}$  column of  $\mathbf{Q}$ . The number of elements in  $\{c^{k+1}\}$  corresponds to the number of rows in  $\mathbf{P}$ . The number of columns of  $\mathbf{P}$  corresponds to the number of elements in  $\{c^k\}$  and the number of columns of  $\mathbf{Q}$  corresponds to the number of elements in  $\{d^k\}$ . If the columns of  $\mathbf{P}$  and  $\mathbf{Q}$  are adjoined, the result is a square matrix (whose inverse is the matrix with the rows of  $\mathbf{A}$  adjoined below by the rows of  $\mathbf{B}$ ). The number of columns of  $[\mathbf{P} \ \mathbf{Q}]$ , being the number of elements in  $\{c^k\} \cup \{d^k\}$ , is also the number of elements in  $\{c^{k+1}\}$ .

Throughout the remainder of this presentation we shall be using the term **matrix** to refer to the *decomposition* information:  $\mathbf{A}$  and  $\mathbf{B}$ , and the *reconstruction* information:  $\mathbf{P}$  and  $\mathbf{Q}$ , in its entire matrix format; i.e., capable of acting simultaneously on all the information  $\{c^{k+1}\}$ ,  $\{c^k\}$ , and  $\{d^k\}$ , as laid out in vectors, in the manner of equations (2.4), (2.5), and (2.6). We shall be using the term **filter** to refer to the nonzero entries in a representative row of any such matrix, suitable to be applied upon a local portion of the information  $\{c^{k+1}\}$ ,  $\{c^k\}$ , and  $\{d^k\}$ ; e.g. in the manner of equations (2.7), (2.8), and (2.9). We find it convenient to extend the term “filter” to column information as well. Finally we shall be using the term **diagram** to refer to the elements of any instance of a row or column of one of the matrices appearing in the geometric context of the mesh being subdivided and reconstructed; e.g. as shown in Figure 2, Figure 7, and Figure 9. These diagrams may be *simple*; that is, they will only involve nodes and edges of the mesh  $c^{k+1}$ , as in Figures 2 and 7, or they may sometimes be *augmented* for the sake of illustration and explanation; that is, they will also involve nodes and edges of the mesh  $c^k$ , as in Figure 9.

### 3 Coarse and Fine Relationships

The physical situation associated with the segment of the subdivision represented by (2.2) might appear as in Figure 1. To anticipate the approach we shall be taking with surfaces beginning in Section 6, we are

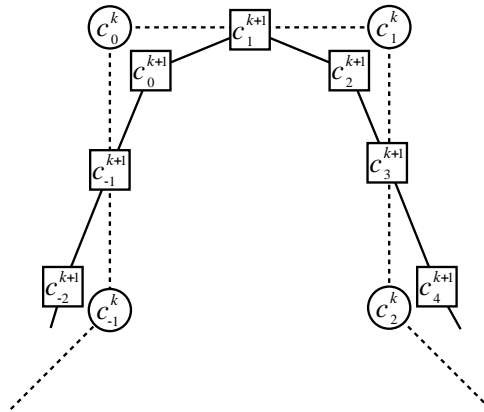


Figure 1: A Physical situation with local indexing

showing a local indexing scheme in this figure. This region of the physical mesh corresponds to the  $j^{\text{th}}$  column of  $\mathbf{P}$  in which the column's nonzero span of entries is centered about row position  $i$ . Both the  $i$  and  $j$  indices of the discussion in Section 2 have been taken as 0 in the diagram, and nearby indices have been renamed relative to this index value. The local view is that  $c_0^{k+1}$  is a fine point upon which we focus

our attention and  $c_0^k$  is the coarse point we hope to estimate based upon  $c_0^{k+1}$  and its neighbors. We have used local indexing in Figure 1 to make the following point: Any selection of distinct indices for distinct points is legal. Rearranging indices permutes rows and columns of  $\mathbf{P}$ , and the ordering of the entries in the vector  $\mathbf{c}^k$ , but only in ways that preserve the product  $\mathbf{P}\mathbf{c}^k$ . The physical configuration of Figure 1 does not change if the points are given new names (which is what re-indexing does). We may use any indexing that assists us, and re-index whenever it is convenient to do so. The diagrams we shall be introducing are impervious to this and, in effect, keep us honest.

In Figure 1 the squares represent the fine points  $\{c^{k+1}\}$ , and the circles represent the coarse points  $\{c^k\}$  in the subdivision  $\mathbf{P}\mathbf{c}^k \rightarrow \hat{\mathbf{c}}^{k+1}$ . The dashed lines connect the points  $\{c^k\}$  to form the coarse mesh, and the solid lines connect the points  $\{c^{k+1}\}$  to form the fine mesh.

This subdivision represents a 2-scale relationship between  $\{c^k\}$  and  $\{c^{k+1}\}$  in which every node  $c_j^k$  of the coarse mesh associates with a *vertex node* (a modified version of  $c_j^k$ ) and an *edge node* (an additionally generated node) in  $\{c^{k+1}\}$ ; that is, the subdivision doubles the number of nodes in interior of the mesh. These nodes may be seen from the rows of the  $\mathbf{P}$  matrix, which appear in pairs, with

$$\frac{1}{8}c_{j-1}^k + \frac{3}{4}c_j^k + \frac{1}{8}c_{j+1}^k \rightarrow c_i^{k+1} \quad (3.1)$$

producing the vertex nodes and

$$\frac{1}{2}c_j^k + \frac{1}{2}c_{j+1}^k \rightarrow c_{i+1}^{k+1} \quad (3.2)$$

producing the edge nodes. The identification of  $\frac{1}{8}c_{j-1}^k + \frac{3}{4}c_j^k + \frac{1}{8}c_{j+1}^k$  as a slightly modified version of  $c_j^k$  should be clear from the coefficients. In Figure 1  $c_{-2}^{k+1}$ ,  $c_0^{k+1}$ ,  $c_2^{k+1}$ , and  $c_4^{k+1}$  are examples of vertex nodes while  $c_{-1}^{k+1}$ ,  $c_1^{k+1}$ , and  $c_3^{k+1}$  are examples of edge nodes.

For some subdivisions, such as the one due to Chaikin (corresponding to quadratic B-spline subdivision):

$$\frac{3}{4}c_{j-1}^k + \frac{1}{4}c_j^k \rightarrow c_{i-1}^{k+1} \quad (3.3)$$

$$\frac{1}{4}c_{j-1}^k + \frac{3}{4}c_j^k \rightarrow c_i^{k+1} \quad (3.4)$$

the choice of which of  $c_{i-1}^{k+1}$  and  $c_i^{k+1}$  is a vertex node and which is an edge node is arbitrary. However, if the choice is made consistently with every pair of points, all points can be handled by a single, consistent row pattern in  $\mathbf{A}$  and  $\mathbf{B}$  and a single, consistent column pattern in  $\mathbf{Q}$ .

Not all subdivisions are 2-scale. In the later sections on triangular-mesh surfaces, for example, the subdivisions all represent 4-scale relationships with one vertex node to every three edge nodes. Additionally, around extraordinary points in a mesh, the number of vertex and edge nodes generated by the subdivision may vary locally.

## 4 Diagrammatic View of Curve Subdivision

In generating subdivision reversal on non-tensor-product meshes, it is better to abandon matrix notation in favor of something else. We have found certain diagrams to be the most useful tools, and we introduce them in this section in the simple case of curve subdivisions.

In the review of Section 2 it should be noted that the processes of the construction can be accomplished using *columns* of  $\mathbf{P}$ , *columns* of  $\mathbf{Q}$ , *rows* of  $\mathbf{A}$ , and *rows* of  $\mathbf{B}$ . Each element of these rows and columns stands in one-to-one correspondence with an element of the fine mesh  $\{c^{k+1}\}$ , so that each of our diagrams can consist of a collection of nodes on the fine mesh labelled with the values from a row of  $\mathbf{A}$  or  $\mathbf{B}$  or from a column of  $\mathbf{P}$  or  $\mathbf{Q}$ . The interpretation of each diagram will reflect the role that the row or column plays in the matrix-matrix products of (2.3) and matrix-vector products of (2.6), (2.5), (2.4), and (2.1).

#### 4.1 The $\mathbf{P}$ Column Diagram

We continue to illustrate our discussion with cubic B-spline curve subdivision and introduce its  $\mathbf{P}$  column diagram in Figure 2. As the name suggests, this diagram simply represents one of the columns of the  $\mathbf{P}$

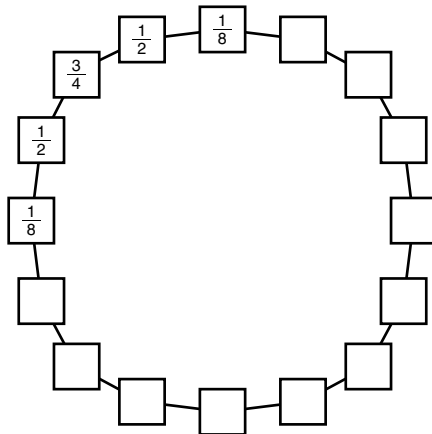


Figure 2: Cubic B-spline curve subdivision  $\mathbf{P}$  diagram

matrix, let us choose the  $j^{\text{th}}$ , with the nonzero values in that column written over the elements  $c_{i-2}^{k+1}$ ,  $c_{i-1}^{k+1}$ ,  $c_i^{k+1}$ ,  $c_{i+1}^{k+1}$ ,  $c_{i+2}^{k+1}$  of  $\{c^{k+1}\}$  to which they correspond.

It should be understood that diagrams such as Figure 2 present an idealized view of the physical situation. Our diagrams show the point-edge association (that is, the connectivity) of the points (in the case of Figure 2 for a closed curve). The physical position of the points in space may appear quite differently; e.g. as in Figure 1. The diagrams will merely assist us in composing equations that will be solved for the  $\mathbf{A}$ ,  $\mathbf{B}$ , and  $\mathbf{Q}$  filters.

We may stylize Figure 1 to produce the *augmented*  $\mathbf{P}$  column diagram shown in Figure 3. Such augmentation is not needed in the construction, but it does help to explain how to interpret the  $\mathbf{P}$  column diagram of Figure 2. The augmentation is accomplished by rendering nodes and edges for the coarse mesh  $\{c^k\}$  together with nodes and edges for the fine mesh  $\{c^{k+1}\}$  of Figure 2. The augmentation may be further embellished by shading the node corresponding to  $c_j^k$  in the coarse mesh. Since  $\mathbf{P}$  is a mapping from the coarse mesh to the fine mesh, with each column of  $\mathbf{P}$  corresponding to a coarse element  $c_j^k$ , the augmentation contains the full description of column  $j$  of matrix  $\mathbf{P}$  in a purely graphical format without the need for explicit indices.

Figure 3, displays the  $\mathbf{P}$  filter of the subdivision in the following way: the number in each square (fine point) represents the contribution that the shaded circle (the designated coarse point) makes to that fine point in the subdivision. Squares (fine points) not influenced by the shaded circle (that is, associated with

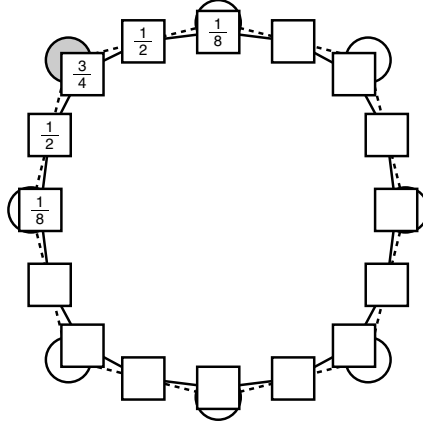


Figure 3: Augmented  $\mathbf{P}$  column diagram

$\mathbf{P}$  filter values that are zero) are left blank and, at our discretion to simplify later diagrams, may not even be shown. In the product  $\mathbf{P}\mathbf{c}^k \rightarrow \hat{\mathbf{c}}^{k+1}$  Figure 3 describes exactly how the element  $c_j^k$  contributes to the result  $\hat{\mathbf{c}}^{k+1}$ , as is shown in equation (4.1.1).

$$\begin{aligned}
 \hat{c}_{i-2}^{k+1} &= \frac{1}{8} c_j^k + \dots \\
 \hat{c}_{i-1}^{k+1} &= \frac{1}{2} c_j^k + \dots \\
 \hat{c}_i^{k+1} &= \frac{3}{4} c_j^k + \dots \\
 \hat{c}_{i+1}^{k+1} &= \frac{1}{2} c_j^k + \dots \\
 \hat{c}_{i+2}^{k+1} &= \frac{1}{8} c_j^k + \dots
 \end{aligned} \tag{4.1.1}$$

Equation (4.1.1) gives all the elements of  $\hat{\mathbf{c}}^{k+1}$ , and only the elements of  $\hat{\mathbf{c}}^{k+1}$ , to which  $c_j^k$  contributes.

If a different circle were chosen as  $c_j^k$  to be shaded in Figure 3, the numbers would shift along the  $\mathbf{P}$  diagram appropriately, since the different coarse point would contribute to different fine points. This reflects the way in which the nonzero elements shift upwards or downwards as we progress from column to column in the  $\mathbf{P}$  matrix. Figure 6 involves such shifting for five consecutive choices of coarse points.

## 4.2 The $\mathbf{A}$ Row Diagram

The  $\mathbf{A}$  matrix, a section of which is given in (2.12), maps from  $\{c^{k+1}\}$  to  $\{c^k\}$ . Each row corresponds to an element  $c_j^k$  of the coarse mesh, and each entry in a row corresponds to an element  $c_i^{k+1}$  of the fine mesh. Figure 4 shows this as an  $\mathbf{A}$  row diagram. This diagram can be augmented, too, as in Figure 5, which shows  $c_j^k$  as the shaded circle.

Figure 4 and Figure 5 contain the entries of row  $j$  as unknown symbols, as they would appear at the start of constructing the equations  $\mathbf{A}\mathbf{P} = \mathbf{I}$ . The symbol in each square represents how much of the corresponding fine point is accumulated to produce the designated coarse point; that is, Figure 4, and its augmented version Figure 5, correspond to the following equation arising from the interaction of the  $j^{\text{th}}$  row of matrix  $\mathbf{A}$  with the column  $\mathbf{c}^{k+1}$ :

$$c_j^k = a_{i-3} c_{i-3}^{k+1} + a_{i-2} c_{i-2}^{k+1} + a_{i-1} c_{i-1}^{k+1} + a_i c_i^{k+1} + a_{i+1} c_{i+1}^{k+1} + a_{i+2} c_{i+2}^{k+1} + a_{i+3} c_{i+3}^{k+1} \tag{4.2.1}$$

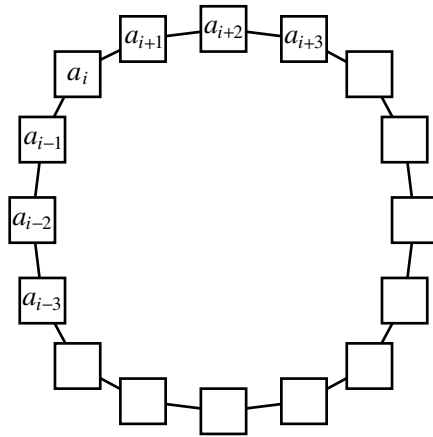


Figure 4: Cubic B-spline curve subdivision **A** diagram

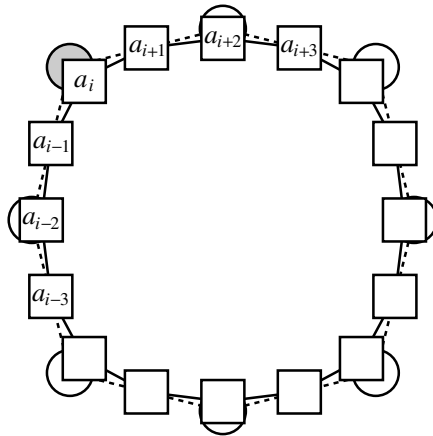


Figure 5: Augmented **A** row diagram

What is more important, however, is the interaction of a local sequence of the columns of matrix **P**, centered around  $j^{\text{th}}$  column, with the  $j^{\text{th}}$  row of matrix **A**. This interaction is presented in Figure 6, where five successive **P** column diagrams are shown in conjunction with the  $j^{\text{th}}$  **A** row diagram. These diagrams have been augmented with the coarse mesh  $\{c^k\}$  shown as circles, the shaded circle showing which coarse point corresponds to the **P** column elements and the emboldened circle showing the coarse point corresponding to the **A** row elements.

Each conjunction represents one of the nontrivial equations comprising  $\mathbf{AP} = \mathbf{I}$ , an equation given by forming the products of overlapping **P** and **A** entries and summing up all products. The numbering of the diagrams corresponds to the ordering shown for the equations (4.2.2) that they generate, with the number of the diagram corresponding to the number of the equation, reading from top to bottom. Since all **A** rows are identical in the interior situation shown for the mesh, each **A** row diagram may be interpreted as

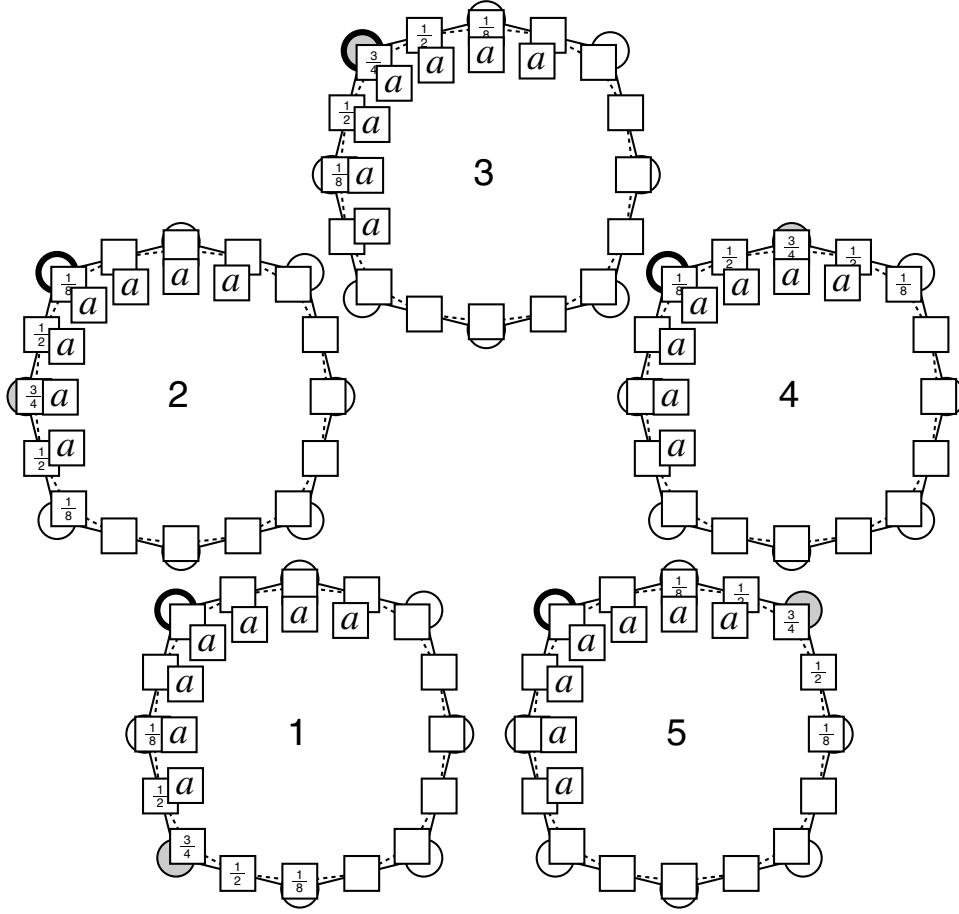


Figure 6:  $\mathbf{A} \times \mathbf{P}$  interactions for cubic B-spline subdivision

involving the same  $\mathbf{A}$  entries given in (4.2.1), and consequently, the equations represented by Figure 6:

$$\begin{aligned}
 \frac{1}{2} a_{i-3} + \frac{1}{8} a_{i-2} &= 0 \\
 \frac{1}{2} a_{i-3} + \frac{3}{4} a_{i-2} + \frac{1}{2} a_{i-1} + \frac{1}{8} a_i &= 0 \\
 \frac{1}{8} a_{i-2} + \frac{1}{2} a_{i-1} + \frac{3}{4} a_i + \frac{1}{2} a_{i+1} + \frac{1}{8} a_{i+2} &= 1 \quad (4.2.2) \\
 \frac{1}{8} a_i + \frac{1}{2} a_{i+1} + \frac{3}{4} a_{i+2} + \frac{1}{2} a_{i+3} &= 0 \\
 \frac{1}{8} a_{i+2} + \frac{1}{2} a_{i+3} &= 0
 \end{aligned}$$

are generic for the entire interior of the mesh. These are precisely the equations represented by (2.10). The particular diagram in Figure 6 that yields the right hand side value of 1 rather than 0 comes when the  $\mathbf{A}$  row diagram and the  $\mathbf{P}$  column diagram correspond to the same coarse point; namely, the third of the five diagrams.

Solving these equations yields the  $a_{i-3}, \dots, a_{i+3}$  values appearing in the  $\mathbf{A}$  row diagram shown in Figure 7. These are, of course, the values in (2.11) and (2.12), since the equations (4.2.2) produced

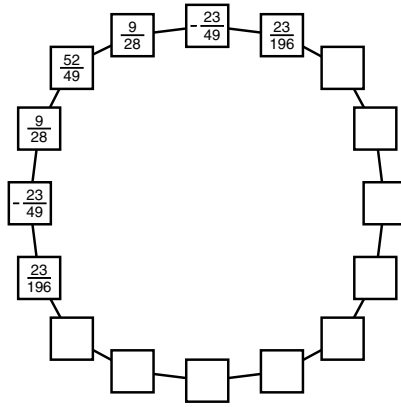
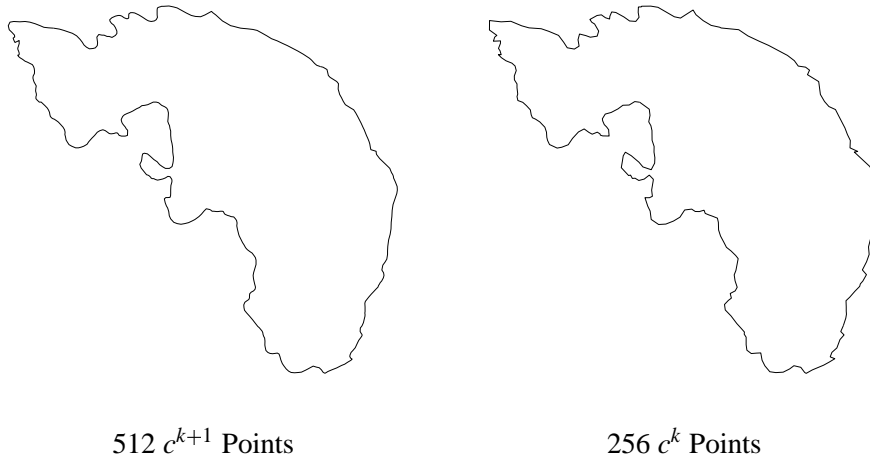


Figure 7: Cubic B-spline subdivision A row diagram of width 7

diagrammically from Figure 6 are designed to be the same as the equations (2.10) produced by matrix multiplication.

In summary, given a set of data  $\{c^{k+1}\}$  such as shown to the left in Figure 8, the diagram in Figure 7 is positioned on each vertex node  $c_i^{k+1}$  in turn, the coordinates of the neighboring points  $c_{i\pm\lambda}^{k+1}$  are multiplied by the  $a$  values sited upon them, the products are summed up, and the result is the coarse point  $c_j^k$  corresponding to the vertex node. If there is no prior information about which nodes are vertex nodes, an arbitrary point may be chosen as one of them, and every other point progressing away from this chosen point may be taken as the rest. This has been done with the points to the left in Figure 8 to produce the points at the right.



512  $c^{k+1}$  Points

256  $c^k$  Points

Figure 8: Shoreline of a Norwegian island

### 4.3 The B and Q Diagrams

The augmented **B** diagram for cubic B-spline curve subdivision is shown at the left in Figure 9. This

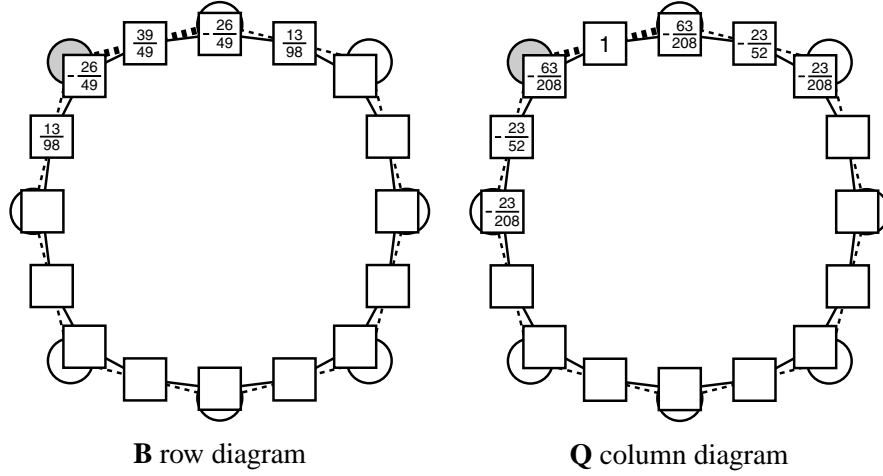


Figure 9: Cubic B-spline subdivision: Augmented **B** and **Q** diagrams

diagram represents a row of the **B** matrix; specifically, that row that creates a  $d$  value contributing to the residuals local to the shaded (coarse) point. The  $d$  value is accumulated by multiplying each fine point by the number written upon it and summing the results; for example from Figure 9:

$$d_\ell^k = \frac{13}{98} c_{i-1}^{k+1} - \frac{26}{49} c_i^{k+1} + \frac{39}{49} c_{i+1}^{k+1} - \frac{26}{49} c_{i+2}^{k+1} + \frac{13}{98} c_{i+3}^{k+1} \quad (4.3.1)$$

The meaning of the  $d_\ell^k$  value is only clear in the context of its corresponding column diagram for **Q**, which is shown at the right in Figure 9. If the coarse points produced by the **A** filter are subdivided using the **P** filter, yielding points  $\{c^{k+1}\}$ , these can be corrected to recover the original  $\{c^{k+1}\}$  points by adding to each individual  $\{c^{k+1}\}$  the products of  $d$  values and **Q** diagram elements. For Figure 9, the partial corrections are:

$$\begin{aligned} c_{i-2}^{k+1} &= \hat{c}_{i-2}^{k+1} - \frac{23}{208} d_\ell^k + \dots \\ c_{i-1}^{k+1} &= \hat{c}_{i-1}^{k+1} - \frac{23}{52} d_\ell^k + \dots \\ c_i^{k+1} &= \hat{c}_i^{k+1} - \frac{63}{208} d_\ell^k + \dots \\ c_{i+1}^{k+1} &= \hat{c}_{i+1}^{k+1} + 1 d_\ell^k + \dots \\ c_{i+2}^{k+1} &= \hat{c}_{i+2}^{k+1} - \frac{63}{208} d_\ell^k + \dots \\ c_{i+3}^{k+1} &= \hat{c}_{i+3}^{k+1} - \frac{23}{52} d_\ell^k + \dots \\ c_{i+4}^{k+1} &= \hat{c}_{i+4}^{k+1} - \frac{23}{208} d_\ell^k + \dots \end{aligned} \quad (4.3.2)$$

With **B** diagrams interpreted in terms of matrix rows and **Q** diagrams interpreted in terms of matrix columns, this also means that the **B** and **Q** diagrams interact in inner-product fashion as do the **P** and **A** diagrams; that is, in the manner of Figure 6, and so the **B** and **Q** diagram diagrams can be used to generate subsets of the equations shown in (2.3).

## 4.4 Diagrams, Cardinality, and Location

We have given the augmented diagrams for the  $\ell^{\text{th}}$  row of  $\mathbf{B}$  and the  $\ell^{\text{th}}$  column of  $\mathbf{Q}$  in Figure 9 in order to draw a few connections between the  $\mathbf{B}$  and  $\mathbf{Q}$  diagrams and the cardinality of the spaces behind the decomposition and reconstruction operations. These observations are not only based on the cubic B-spline example but hold true on all of the subdivisions that we have explored.

Our example subdivision doubles the cardinality of the points. Each  $c_j^k$  spawns a vertex node  $c_i^{k+1}$  (an *adjusted* version of the point  $c_j^k$ ) and an edge node  $c_{i+1}^{k+1}$  (a *newly created* point associated with  $c_j^k$ ). The intent of a multiresolution, which we construct by reversing the subdivision, is to represent the information about the fine points  $\{c^{k+1}\}$  using only an equal number of locations to store both the coarse points  $\{c^k\}$  and the difference information  $\{d^k\}$ . More accurately, the  $\{c^k\}$  information must require storage equal to that of the vertex nodes in  $\{c^{k+1}\}$ , and the difference information must occupy the storage equal to that of the edge nodes. If more than one edge node is created for each vertex node, we still wish this storage model to hold.

Subdivision moves us from a space  $\mathcal{V}^k$  of cardinality  $v^k$  to a space  $\mathcal{V}^{k+1}$  of cardinality  $v^{k+1}$ . The space  $\mathcal{V}^{k+1}$  has an alternative representation as  $\mathcal{V}^k + \mathcal{W}^k$ , where the complementary space  $\mathcal{W}^k$  is of cardinality  $w^k$ . This alternative representation is reflected in the observation that there are  $v^k$  columns in the  $\mathbf{P}$  matrix connected to the  $v^k$  coarse points  $\{c^k\}$  and  $w^k$  columns in the  $\mathbf{Q}$  matrix connected to the  $w^k$  elements of detail data  $\{d^k\}$ .

Correspondingly, we note that  $v^k$  diagrams for the  $\mathbf{P}$  matrix are matched with  $w^k$  diagrams for the  $\mathbf{Q}$  matrix. Each  $\mathbf{P}$  diagram is associated uniquely with one of the  $v^k$  points of  $\{c^k\}$ , each  $\mathbf{Q}$  diagram is associated with one of the  $w^k$  points of  $\{c^{k+1}\} \setminus \{c^k\}$ . The  $\mathbf{P}$  diagram resides centrally on a fine point that we consider to be an adjusted coarse point, and the  $\mathbf{Q}$  diagram resides centrally on a fine point that we consider to be newly generated by the subdivision; that is, associated with one of the edges of the  $\{c^k\}$  mesh. We have emboldened the appropriate edge of the augmented column diagram for  $\mathbf{Q}$  in Figure 9.

The cardinalities and diagram localities that we see for  $\mathbf{P}$  and  $\mathbf{Q}$  are, respectively, echoed by  $\mathbf{A}$  and  $\mathbf{B}$ . The  $\mathbf{A}$  diagram, representing row  $j$  of the  $\mathbf{A}$  matrix and centered on the fine point  $c_i^{k+1}$  of the diagram, corresponds to the coarse point  $c_j^k$  that is produced by applying the  $a$  values to the fine points at diagram position  $i$  and its neighbors, the points on which the  $a$  values are written, and summing the results. The diagram for  $\mathbf{B}$ , representing row  $\ell$  of the  $\mathbf{B}$  matrix, is centered on a fine point  $c_{i+1}^{k+1}$  that is newly generated by the subdivision. It represents one of the fine points primarily influenced by the  $\ell^{\text{th}}$  element of detail information  $\{d^k\}$ . We have emboldened the appropriate edge of the augmented row diagram for  $\mathbf{B}$  in Figure 9.

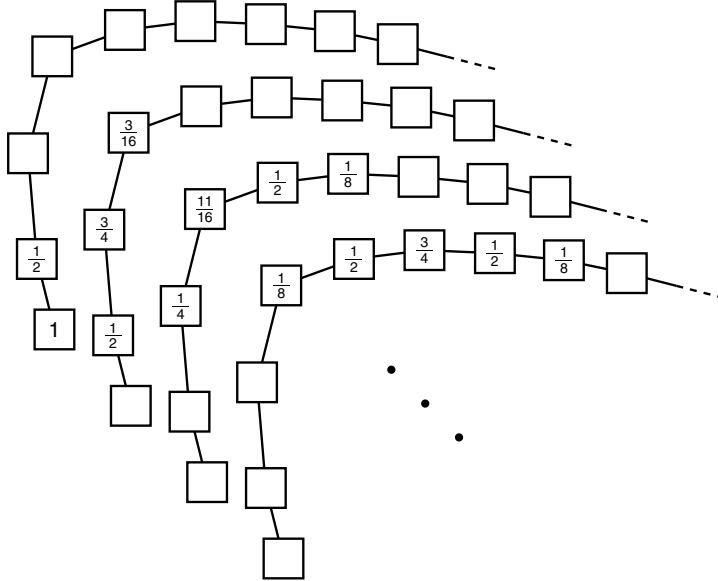
These observations have held true at the interior points of any mesh we have worked with. They break slightly on or near the boundary of a mesh, but they still provide useful geometric insights.

## 5 At the Boundary

The subdivision that is being used as an example is provided by midpoint insertion on cubic B-splines with uniformly-spaced knots of multiplicity one, at least with regards to the interior of the parameter range. At the ends of the range, corresponding to the beginning and ending points of any curve that these B-splines might generate, it is a common practice to terminate the B-splines with knots of four-fold multiplicity. This convention provides that any curve terminates upon the extreme control points  $c_{\min}^{k+1}$  and  $c_{\max}^{k+1}$  without any restriction on the behavior of the curve in the neighborhood of these points. The first and last segments of the curve, in other words, may be completely and generally cubic.

## 5.1 Boundary $\mathbf{P}$ Diagrams

Using the endpoint knot convention just described, and the midpoint knot-insertion definition of subdivision, the first four  $\mathbf{P}$  diagrams representing that subdivision are shown in Figure 10. The first three diagrams, corresponding to the first three columns of the  $\mathbf{P}$  matrix are special. The fourth diagram (column) has already assumed the character of the interior diagrams (columns).



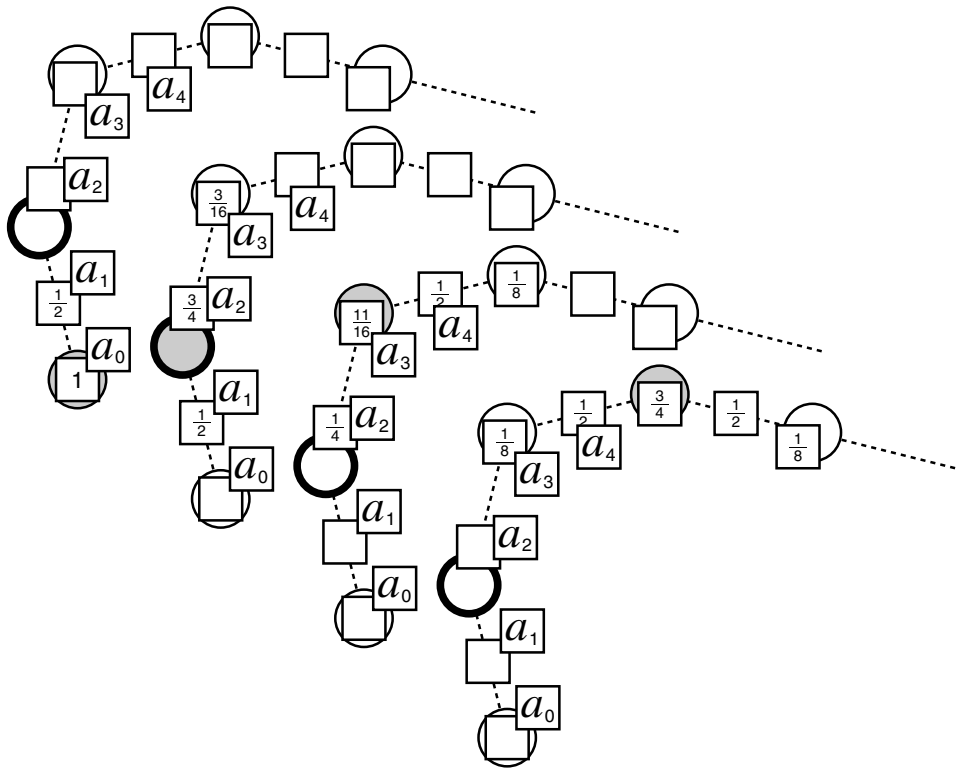


Figure 12: The (augmented) arrangement for determining equations for the second **A** diagram

## 5.2 Boundary **A** Diagrams

Figure 11 shows the **P** and **A** interactions necessary to generate the equations for the beginning **A** filter. This is the **A** filter that estimates the initial point of the coarse mesh  $c_{\min}^k$ . Any width of **A** filter can be investigated, but here the width is minimal. With the filter consisting of only  $a_0$ , the only interaction with **P** corresponds to the first **P** diagram (column).

By the way the subdivision is defined at the boundary, investigating a minimal **A** filter is the obvious thing to do, since the subdivision simply reproduces the extreme points of the mesh  $c_{\min}^k = c_{\min}^{k+1}$ . Nevertheless, for completeness, the setup for determining that, in fact,

$$c_{\min}^k = a_0 c_{\min}^{k+1} \Rightarrow a_0 = 1$$

is what is given in Figure 11.

The second **A** diagram, for estimating the second point of the coarse mesh, is more interesting and is given in Figure 12. The augmentation of the diagram shows the coarse point to be estimated (with a bold margin) as well as the coarse points corresponding to each **P** diagram (shaded). The **A** diagram being investigated is five elements long, which is the closest possible to the seven-element filter being used for the interior points this near to the boundary. It is also centered over the vertex point associated with the coarse point to be estimated.

For the five-element **A** diagram being investigated, there are only four relevant **P** diagrams, and the equations that are generated by multiplying the numeric/symbolic labels of corresponding fine points and

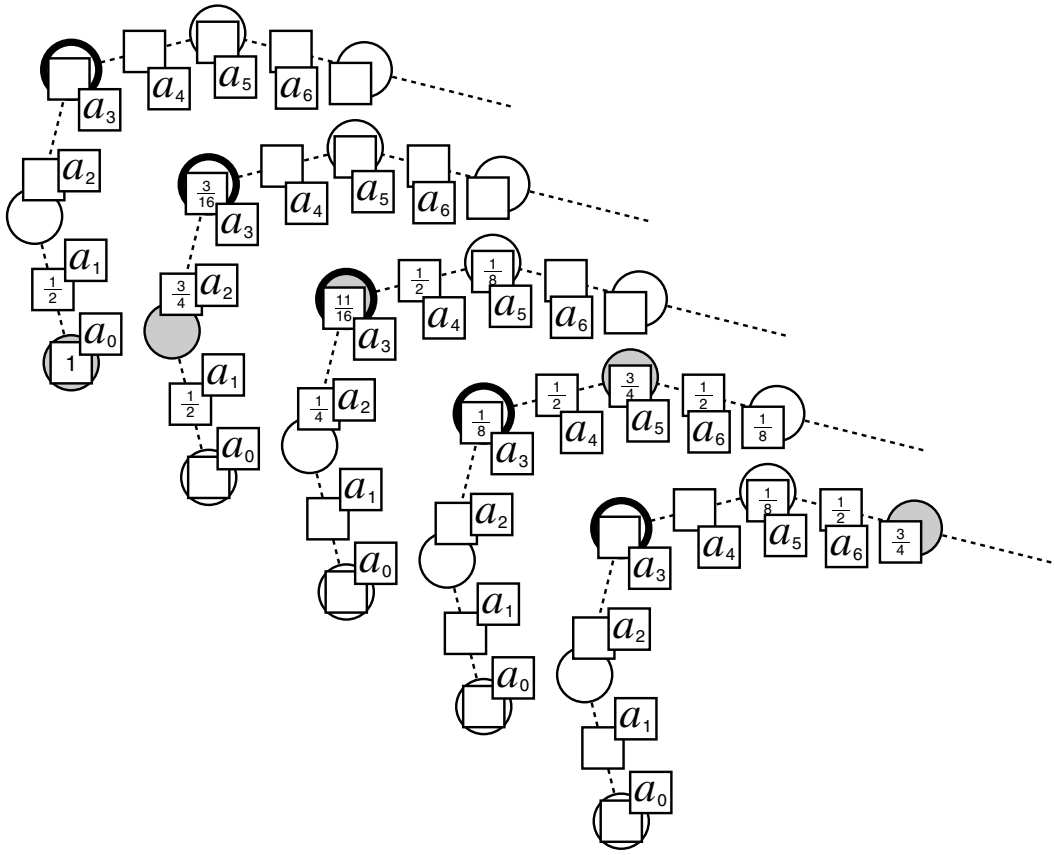


Figure 13: The (augmented) arrangement for determining equations for the third **A** diagram

summing are:

$$\begin{aligned}
 1 a_0 + \frac{1}{2} a_1 &= 0 \\
 \frac{1}{2} a_1 + \frac{3}{4} a_2 + \frac{3}{16} a_3 &= 1 \\
 \frac{1}{4} a_2 + \frac{11}{16} a_3 + \frac{1}{2} a_4 &= 0 \\
 \frac{1}{8} a_3 + \frac{1}{2} a_4 &= 0
 \end{aligned} \tag{5.2.1}$$

The second row-column interaction is set to 1, because this construction is to determine the second coarse point, and it is the second **P** diagram that corresponds to that point.

The setup for determining the next **A** diagram in order is shown in Figure 13. The result of the entire exercise is shown in Figure 14.

### 5.3 Boundary **B** and **Q** Diagrams

To establish **B** diagrams near the boundary, we proceed in the way we did for **A** diagrams. To begin, we would try solving for the closest diagram to the boundary that we could associate symmetrically with the



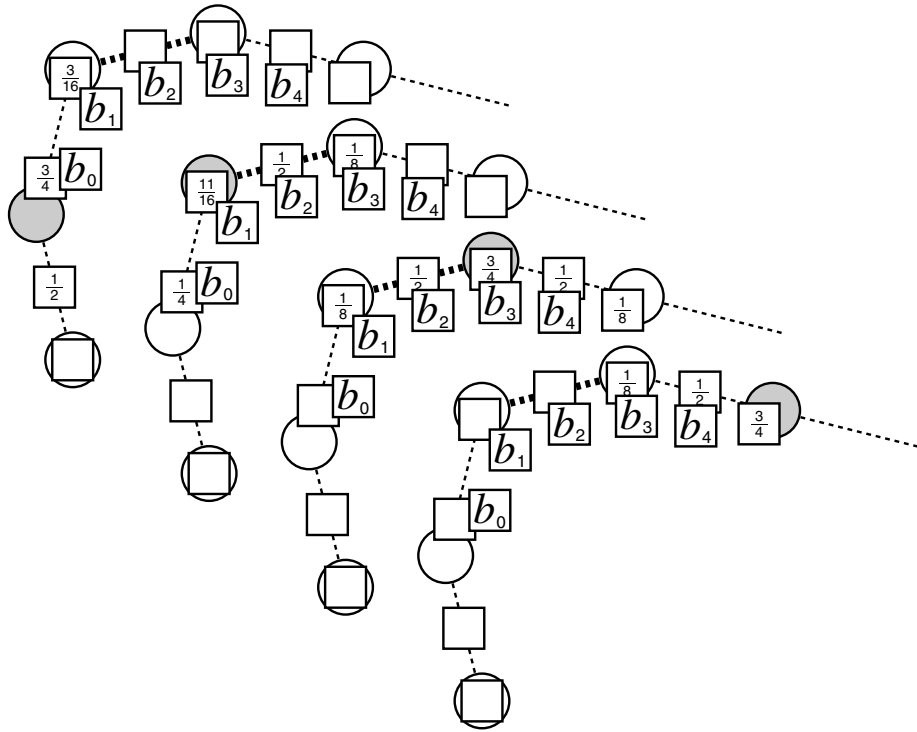


Figure 16: Constructing the third (second nontrivial) boundary **B** diagram

that position. This recipe would lead to a 3-node diagram centered on the fine node in Figure 15 between the first two coarse nodes. The nature of the boundary subdivision being as it is, however, replicating the first coarse node as the first fine node and thereby incurring no error in this immediate location, this diagram turns out to yield null elements in the solution of the equations that are produced.

Therefore to save space, Figure 15 shows the first **B** diagram configuration that yields nontrivial elements. The interactions of such a diagram with the boundary **P** diagrams contribute to the equations  $\mathbf{BP} = \mathbf{0}$ . Figure 15, for example, would contribute

$$\begin{aligned}
 1 b_0 + \frac{1}{2} b_1 &= 0 \\
 \frac{1}{2} b_1 + \frac{3}{4} b_2 + \frac{3}{16} b_3 &= 0 \\
 \frac{1}{4} b_2 + \frac{11}{16} b_3 + \frac{1}{2} b_4 &= 0 \\
 \frac{1}{8} b_3 + \frac{1}{2} b_4 &= 0
 \end{aligned} \tag{5.3.1}$$

Figure 16 continues this construction for the second boundary **B** diagram, centered on the edge node of the third edge of the mesh. This figure will contribute the equations

$$\begin{aligned}
 \frac{3}{4} b_0 + \frac{3}{16} b_1 &= 0 \\
 \frac{1}{4} b_0 + \frac{11}{16} b_1 + \frac{1}{2} b_2 + \frac{1}{8} b_3 &= 0
 \end{aligned} \tag{5.3.2}$$

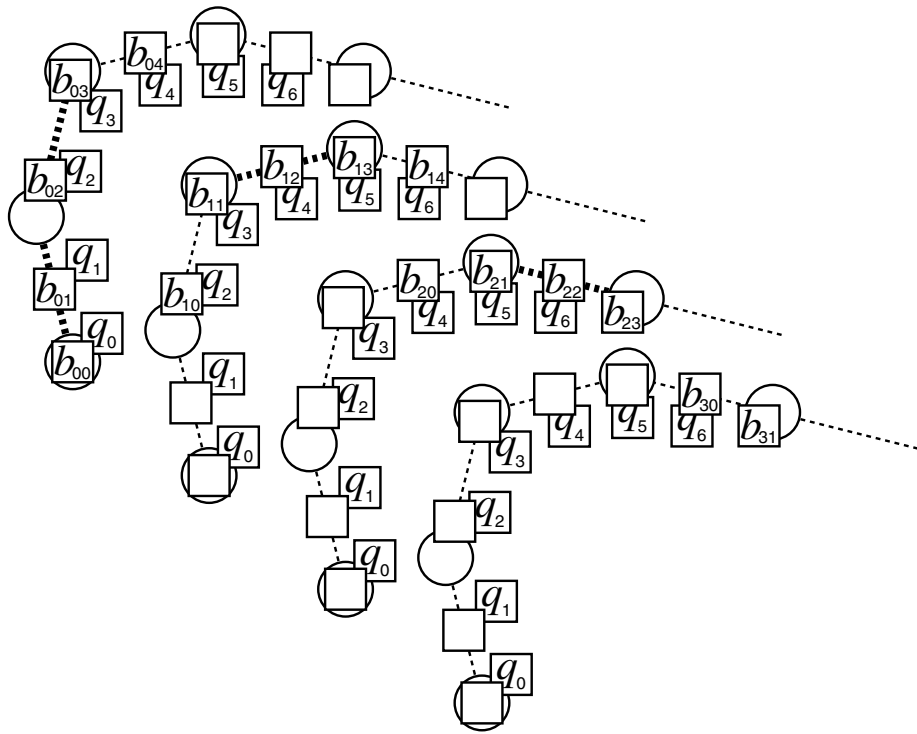


Figure 17: Boundary patterns contributing to  $\mathbf{BQ} = \mathbf{I}$

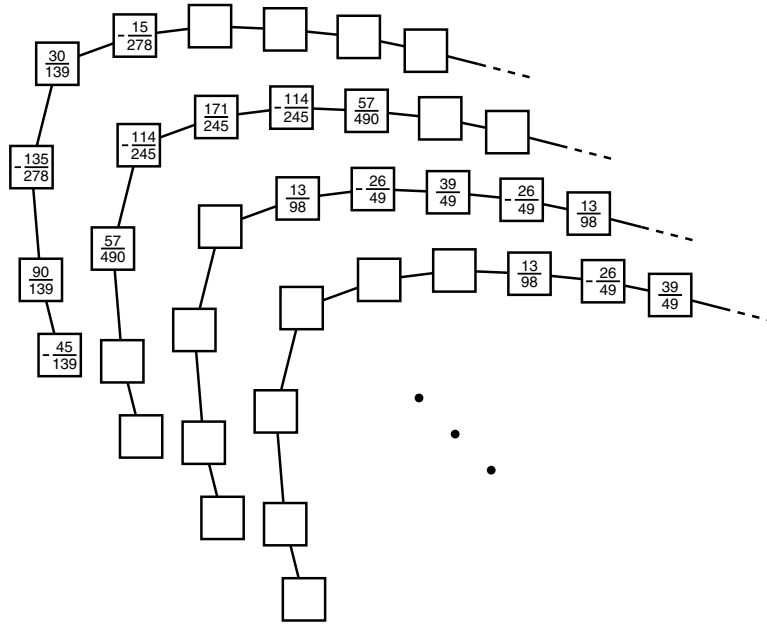


Figure 18:  $\mathbf{B}$  diagrams at the boundary

$$\frac{1}{8}b_1 + \frac{1}{2}b_2 + \frac{3}{4}b_3 + \frac{1}{2}b_4 = 0$$

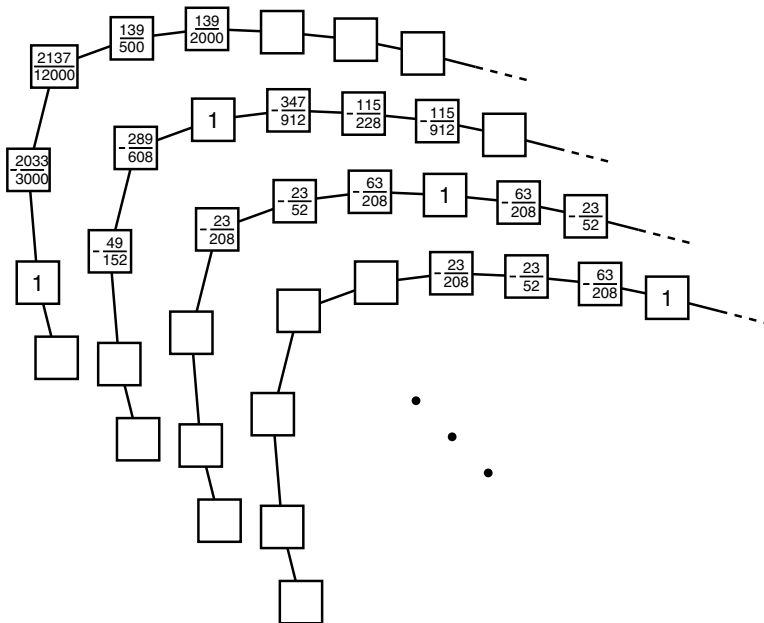


Figure 19:  $\mathbf{Q}$  diagrams at the boundary

$$\frac{1}{8}b_3 + \frac{1}{2}b_4 = 0$$

Trial diagrams of this character will be set up to generate the equations  $\mathbf{A}\mathbf{Q} = \mathbf{0}$ . The diagram constructions will look similar to Figures 15 and 16, with the elements of the  $\mathbf{A}$  diagrams replacing those of the  $\mathbf{P}$  diagrams and symbols  $q$  replacing symbols  $b$ . To give a different flavor, Figure 17 shows the set up for contributing to the equations  $\mathbf{B}\mathbf{Q} = \mathbf{I}$  from a  $\mathbf{Q}$  diagram of length 7 centered with respect to the second edge and its interaction with the first 4 nontrivial  $\mathbf{B}$  diagrams.

When all equations have been generated and solved, proceeding as we have done in terms of the lengths chosen for the boundary diagrams, we obtain the boundary  $\mathbf{B}$  diagrams shown in Figure 18 and the boundary  $\mathbf{Q}$  diagrams shown in Figure 19.

## 6 Diagrammatic View of Triangular Mesh Subdivision

The subdivisions we shall be considering here, the Butterfly subdivision of Dyn, Levin, and Gregory [3], Loop's subdivision [7], and a subdivision proposed by Litke, Schröder, et. al. [6], will be applied to regular, triangular meshes. These subdivisions convert a coarse mesh representing points  $\{c^k\}$  into a finer mesh representing points  $\{c^{k+1}\}$ , as is shown in Figure 20. One edge node is generated for each edge joining two points in  $\{c^k\}$ . And each point of  $\{c^k\}$  is adjusted to produce a vertex node. In Figure 20 the original  $\{c^k\}$  mesh nodes are circles and they reappear in their  $\{c^{k+1}\}$  vertex-node form as circles again in the figure. The  $\{c^{k+1}\}$  edge nodes are shown as boxes. Thus, the cardinality of  $\mathcal{V}^k$  (or  $\{c^k\}$ , or  $\mathbf{P}$ , or  $\mathbf{A}$ ) is " $n$ " and the cardinality of  $\mathcal{V}^{k+1}$  (or  $\{c^{k+1}\}$ ) is " $4n$ ". Correspondingly, the cardinality of  $\mathcal{W}^k$  (or  $\{d^k\}$ , or  $\mathbf{Q}$ , or  $\mathbf{B}$ ) is " $3n$ ".

The local indexing scheme that we have found most useful for diagrams on such triangular meshes is the spiral one indicated in Figure 21 using an  $\mathbf{A}$  diagram as an example. To measure the size of a diagram,

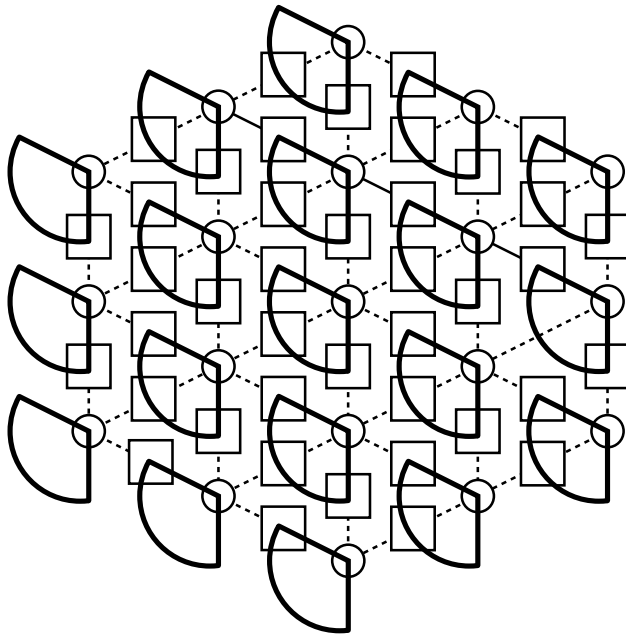


Figure 20: Cardinality in triangular mesh subdivision

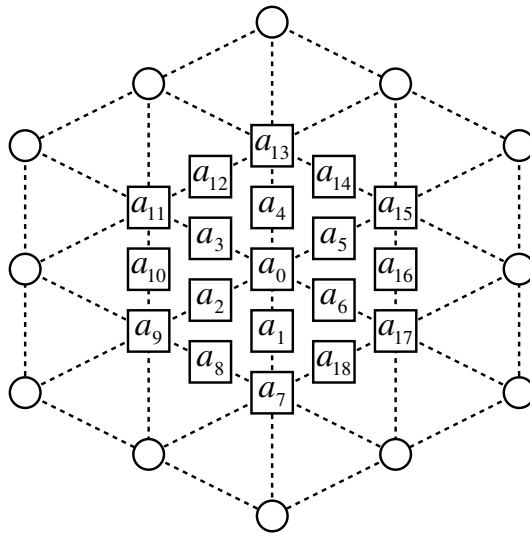


Figure 21: Spiral indexing, as shown on an  $\mathbf{A}$  diagram

we use the term *width* to refer to the number of complete spiral cycles contained in the diagram. Figure 21 has width 2. If the diagram stopped with the entry  $a_6$ , it would have width 1. If the diagram only contained the element  $a_0$ , it would have width 0. A diagram of width 3 would carry on to include  $a_{36}$ , and so on. In this we are employing an existing concept of *topological distance* and the *topological neighborhood* of a vertex [9], and our spiral index convention simply imposes a sequencing on that concept.

As in the case of curves, the  $\mathbf{A}$  diagram of Figure 21 represents a row of an underlying  $\mathbf{A}$  matrix,

with only the nonzero elements of that row being depicted. It would be interpreted as specifying how the coarse point  $c_0^k$  at location 0 (hidden as a circle under the square of  $a_0$ ) would be extracted from the fine points  $c_0^{k+1}, \dots, c_{18}^{k+1}$  shown as the squares; namely, as the sum of each of these fine points times its corresponding  $a$  factor in the style of (4.2.1):

$$a_0 c_0^{k+1} + \dots + a_{18} c_{18}^{k+1} \rightarrow c_0^k$$

The essence of developing an  $\mathbf{A}$  diagram, just as was the case for curves, involves specifying inner products of a row of  $\mathbf{A}$  (populated with unknowns) with columns of  $\mathbf{P}$ , equating one of these inner products to 1 and the remaining products to 0 appropriately, and solving for the elements of the row of  $\mathbf{A}$ . Transcribed into the realm of diagrams, a typical inner product between a row of  $\mathbf{A}$  and a column of  $\mathbf{P}$  would appear as shown in Figure 22 (representing the inner product value  $a_5 p_{24} + a_6 p_{23}$ ). All the inner

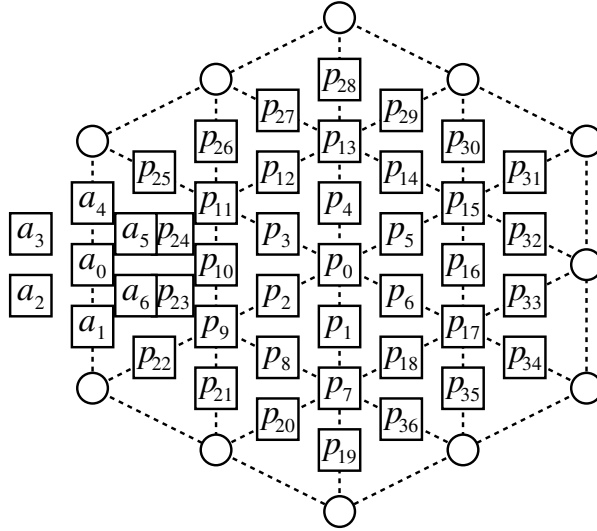


Figure 22: A  $\mathbf{P}$  diagram and  $\mathbf{A}$  diagram inner product

products that are of interest can be found by fixing the position of the  $\mathbf{A}$  diagram and considering, in turn, any  $\mathbf{P}$  diagrams that overlap it in one or more nodes. In the case of the  $\mathbf{A}$  and  $\mathbf{P}$  diagrams, the development outlined for curves would require the inner product to equal 1 for the  $\mathbf{P}$  diagram whose center coincides with the center of the  $\mathbf{A}$  diagram, and it would require the inner product to equal 0 for all other  $\mathbf{P}$  diagram positions, reflecting equation (2.10). The number of equations that are generated in this way, of course, depends on the widths of the  $\mathbf{A}$  and  $\mathbf{P}$  diagrams.

We may also use Figure 22 to describe how a  $\mathbf{P}$  diagram is to be interpreted. As is the case for curves, a  $\mathbf{P}$  diagram shows how much a coarse point contributes in the subdivision to each of the fine points included in the diagram. For Figure 22, this represents the contribution  $p_0 c_0^k$  to  $c_0^{k+1}$  through the contribution  $p_{36} c_0^k$  to  $c_{36}^{k+1}$ .

We have found that  $\mathbf{B}$  and  $\mathbf{Q}$  diagrams, as they did in the curve case, have centers associated with “generated” fine points; that is, with the edge nodes of the fine mesh. Consequently, such diagrams exist in 3 orientations, one aligned along the vertical edges, one along the edges running from lower right to upper left, and one along the edges running from lower left to upper right, as is shown for a generic  $\mathbf{B}$  diagram of width 1 in Figure 23. Note that the spiral indexing of each diagram in this figure is local to the diagram and conforms to its orientation.

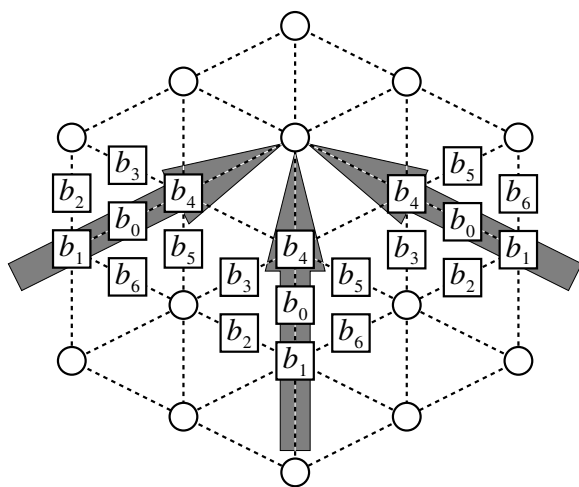


Figure 23: The three basic variants of a **B** diagram of width 1

Changing the  $b$  labels in Figure 23 for  $q$  would produce an equally valid generic **Q** diagram of width 1. The various inner products required to form subsets of equations (2.3) are produced by siting **B** and **Q** diagrams in the style of Figure 23. One site and orientation is chosen for one of the diagrams, and the other diagram is put in all possible positions and orientations locally with respect to the fixed diagram. (For diagrams with symmetries, as we have found ours to be at points well within the interior of meshes, only one position and orientation is needed for the fixed diagram. For more general diagrams, for irregular points, and for the special situations at or near a mesh boundary, it may be necessary to repeat the process for the other representative positions and orientations.) For each distinct pair of locations and orientations, the pairs of  $b$  and  $q$  values found on overlapping nodes are multiplied together in the manner described for Figure 22, and the results are summed. The value is equated to 1 if the two diagrams are sited on the same node and oriented along the same edge, and the value is equated to zero otherwise. To produce subsets of equations (2.3), a fixed position and orientation for the **B** diagram is chosen and tested against all positions of the **P** diagram, multiplying and summing pairs of  $b$  and  $p$  values from overlapping nodes in each position-orientation pair. All sums of products thus formed are equated to 0. Equations (2.3) are approached in the same manner using a fixed-position and orientation of the **Q** diagram and all local positions of the **A** diagram. Again, all sums of products are equated to 0. We have written scripts to do this in the Maple symbolic algebra system [4], and all explicit diagrams that we shall be presenting come from solving the resulting equations in the manner of Section 2, with additional observations to be presented in Section 7.

Figure 24 is included to explain the interpretation of the **B** and **Q** diagrams as filters; that is, their use in creating the detail information  $\mathbf{d}^k$  and the subsequent use of that information to recreate the residuals (2.6). The top diagram of Figure 24 shows a section of the points  $\{c^{k+1}\}$  located about the position indexed by 0. The **B** diagram in the lower left diagram is sited on the position occupied by  $c_6^{k+1}$  and is oriented along the edge joining  $c_0^{k+1}$  and  $c_{17}^{k+1}$ . This **B** diagram is unique to this site. Applying this **B** diagram as a filter to the points corresponds to superimposing the  $b$  and  $c$  diagrams, multiplying the pairs of  $b$  and  $c$  values in overlapping nodes, and summing the results. This produces

$$b_0 c_6^{k+1} + b_1 c_{17}^{k+1} + b_2 c_{18}^{k+1} + b_3 c_1^{k+1} + b_4 c_0^{k+1} + b_5 c_5^{k+1} + b_6 c_{16}^{k+1}$$

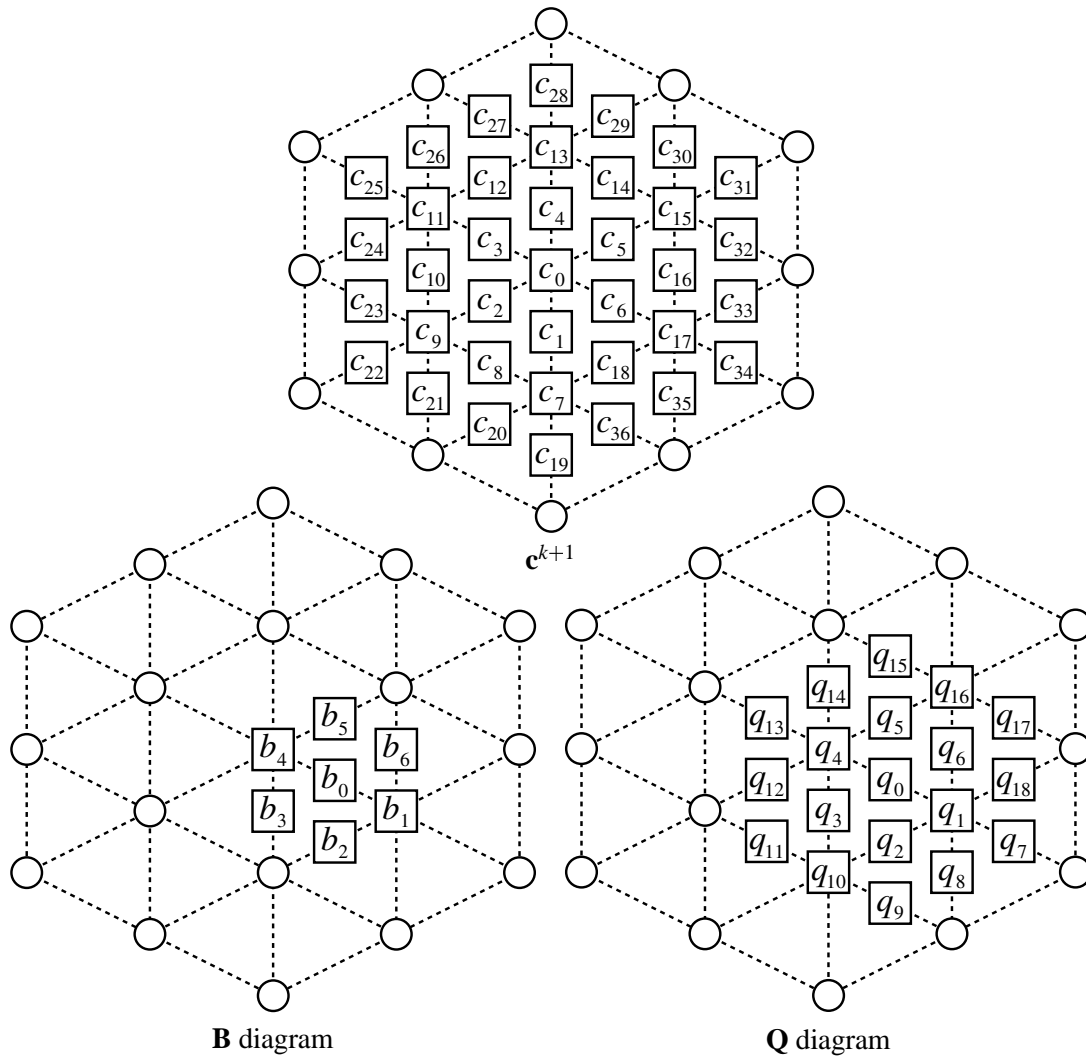


Figure 24: The **B** and **Q** diagrams and the detail information  $\mathbf{d}^k$

which creates the detail value  $d_6^k$ . The **Q** diagram in the lower right diagram is also sited on the position occupied by  $c_6^{k+1}$  and also oriented along the edge joining  $c_0^{k+1}$  and  $c_{17}^{k+1}$ . This **Q** diagram is unique to this site, uniquely associated with the **B** diagram and with the detail value. The detail value  $d_6^k$ , used as a multiplicative factor on the **Q** diagram, produces corrective values to be added to the  $c$  diagram. That is,  $d_6^k$  times the  $q$  diagram is superimposed on the  $c$  diagram, and the  $d_6^k \times q$  value in any box is added to the  $c$  box it overlaps:

$$\begin{array}{cccc}
 d_6^k q_0 + c_6^{k+1}, & d_6^k q_1 + c_{17}^{k+1}, & d_6^k q_2 + c_{18}^{k+1}, & d_6^k q_3 + c_1^{k+1} \\
 d_6^k q_4 + c_0^{k+1}, & d_6^k q_5 + c_5^{k+1}, & d_6^k q_6 + c_{16}^{k+1}, & d_6^k q_7 + c_{34}^{k+1} \\
 \vdots & \vdots & \vdots & \vdots \\
 d_6^k q_{15} + c_{14}^{k+1}, & d_6^k q_{16} + c_{15}^{k+1}, & d_6^k q_{17} + c_{32}^{k+1}, & d_6^k q_{18} + c_{33}^{k+1}
 \end{array}$$

The total correction needed to reconstruct the original value of  $c_5^{k+1}$ , to pick an example point, would involve adding the value of the product  $d_6^k q_5$  above, as well as the values of the  $d_\lambda q_\mu$  products from the nodes resting on location of  $c_5^{k+1}$  using all  $\mathbf{Q}$  diagrams positioned in other nearby locations, in whatever their orientations.

## 7 Problems and Resolution

To carry out the instructions in Section 4.3, the set of equations (2.3) must be solved with versions of  $\mathbf{B}$  and  $\mathbf{Q}$  that have come from solving (2.3). This is done in a context in which these latter two sets of equations are under-determined so that (2.3) contains unknown  $b$  and  $q$  values. As a consequence,  $\mathbf{BQ} = \mathbf{I}$ ; that is, equation (2.3), is not a linear set of equations but a bilinear one. It involves simple products  $b_\lambda \times q_\mu$ . The symbolic algebra system Maple had no difficulty with such equations in the case of curves, apparently because the number of such equations was small. In the case of surface diagrams, however, widths of  $\mathbf{B}$  and/or  $\mathbf{Q}$  diagrams larger than 2 has usually resulted in failure for us. Either Maple would report that no solution could be found (in situations where subsequently solutions were, in fact, found by the approach to be described here), or Maple would simply run without terminating and would have to be eventually halted. A reformulation of this system of equations in the symbolic algebra system Mathematica [11] yielded no better results. Since the widths of the  $\mathbf{B}$  and  $\mathbf{Q}$  diagrams grow in size reflecting the width of the  $\mathbf{A}$  diagram, this appeared to doom our approach to produce nothing but trivial multiresolution filters, generally having  $\mathbf{A}$  diagrams of widths no more than 1 or 2.

Ultimately, we resolved the impasse by considering the lifting process [10]. In matrix terms, lifting simply observes that, if

$$\begin{bmatrix} \mathbf{A} \\ \dots \\ \mathbf{B} \end{bmatrix} \times \begin{bmatrix} \mathbf{P} & \vdots & \mathbf{Q} \end{bmatrix} = \begin{bmatrix} \mathbf{I} & \vdots & \mathbf{0} \\ \dots & \cdot & \dots \\ \mathbf{0} & \vdots & \mathbf{I} \end{bmatrix}$$

then also, for a matrix  $\mathbf{S}$  of appropriate dimensions and full rank,

$$\begin{aligned} & \begin{bmatrix} \mathbf{A} - \mathbf{SB} \\ \dots \\ \mathbf{B} \end{bmatrix} \times \begin{bmatrix} \mathbf{P} & \vdots & \mathbf{Q} + \mathbf{PS} \end{bmatrix} \\ &= \begin{bmatrix} \mathbf{AP} - \mathbf{SBP} & \vdots & \mathbf{AQ} + \mathbf{APS} - \mathbf{SBQ} - \mathbf{SBPS} \\ \dots & \cdot & \dots \\ \mathbf{BP} & \vdots & \mathbf{BQ} + \mathbf{BPS} \end{bmatrix} \\ &= \begin{bmatrix} \mathbf{I} & \vdots & \mathbf{0} \\ \dots & \cdot & \dots \\ \mathbf{0} & \vdots & \mathbf{I} \end{bmatrix} \end{aligned}$$

since  $\mathbf{AP} = \mathbf{I}$ ,  $\mathbf{AQ} = \mathbf{0}$ ,  $\mathbf{BP} = \mathbf{0}$ , and  $\mathbf{BQ} = \mathbf{I}$ .

This observation is usually taken as an invitation to find the matrix  $\mathbf{S}$  that converts a known  $\mathbf{Q}$  into a new  $\tilde{\mathbf{Q}} = \mathbf{Q} + \mathbf{PS}$  and a known  $\mathbf{A}$  into a new  $\tilde{\mathbf{A}} = \mathbf{A} - \mathbf{SB}$  so that  $\tilde{\mathbf{A}}$  and  $\tilde{\mathbf{Q}}$  have some better properties with respect to the inner product on the subdivision's underlying function space. Since, by our program, we find a new  $\tilde{\mathbf{A}}$  independently, we use the lifting observation to justify solving for a new  $\tilde{\mathbf{Q}}$  directly from the equations (2.3) using the  $\mathbf{B}$  that was found for the old  $\mathbf{A}$ . In summary, if we can follow our program to solve for  $\mathbf{BQ} = \mathbf{I}$  in a trivial setting, where both  $\mathbf{B}$  and  $\mathbf{Q}$  contain unknowns, then we can fix this version of  $\mathbf{B}$  and use it for all further determinations of  $\mathbf{Q}$  as we explore changes to  $\mathbf{A}$ . Accordingly, for all filters that we present in Sections 8 and 9 it will be seen that only one  $\mathbf{B}$  filter is presented in each section.

## 8 Butterfly Setting

The Butterfly subdivision [2, 12] is interpolatory, is parameterized by a quantity  $w$ , and applies to a regular, triangular mesh. The diagram displaying a column of  $\mathbf{P}$  for this subdivision, is shown in Figure 25 and represents  $w = \frac{1}{16}$ , which is a common choice.

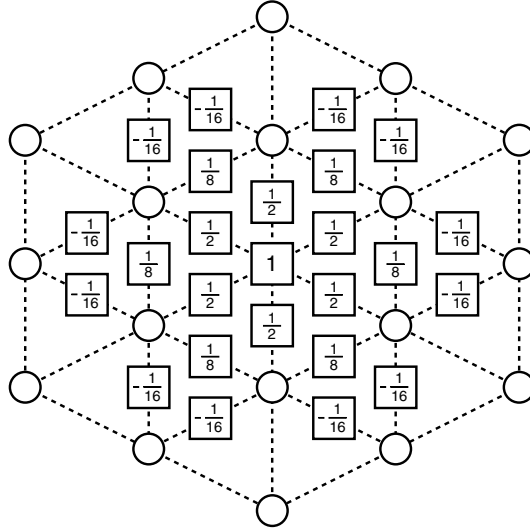


Figure 25: The  $\mathbf{P}$  diagram for Butterfly subdivision

Since Butterfly subdivision is interpolatory, there is a trivial reversal that would simply involve selecting every  $4^{th}$  point from the set  $\{c^{k+1}\}$ , regularly spaced on coarse triangles. To recover the original fine mesh  $\{c^{k+1}\}$ , we merely need to store  $d_\ell^k = \tilde{c}_\ell^{k+1} - c_\ell^{k+1}$  at each of the  $\{c^{k+1}\} \setminus \{c^k\}$  positions. Thus, the original storage of  $\{c^{k+1}\}$  is replaced by the equal amount of storage  $\{c^k\} \cup \{d^k\}$  for this trivial multiresolution. The  $\mathbf{A}$  diagram that represents the sub-selection is shown in Figure 26, along with the corresponding  $\mathbf{B}$  diagram, which merely computes residuals between subdivided coarse points and original fine points at a “generated” (edge-node) location, and the  $\mathbf{Q}$  diagram, which applies that residual to this location. The  $\mathbf{B}$  and  $\mathbf{Q}$  diagrams shown are those associated with the vertical edges of the mesh. It should be remembered that another set of these same diagrams, appropriately rotated, would be associated with the edges running from lower left to upper right, and yet another set would be associated with the edges running from lower right to upper left.

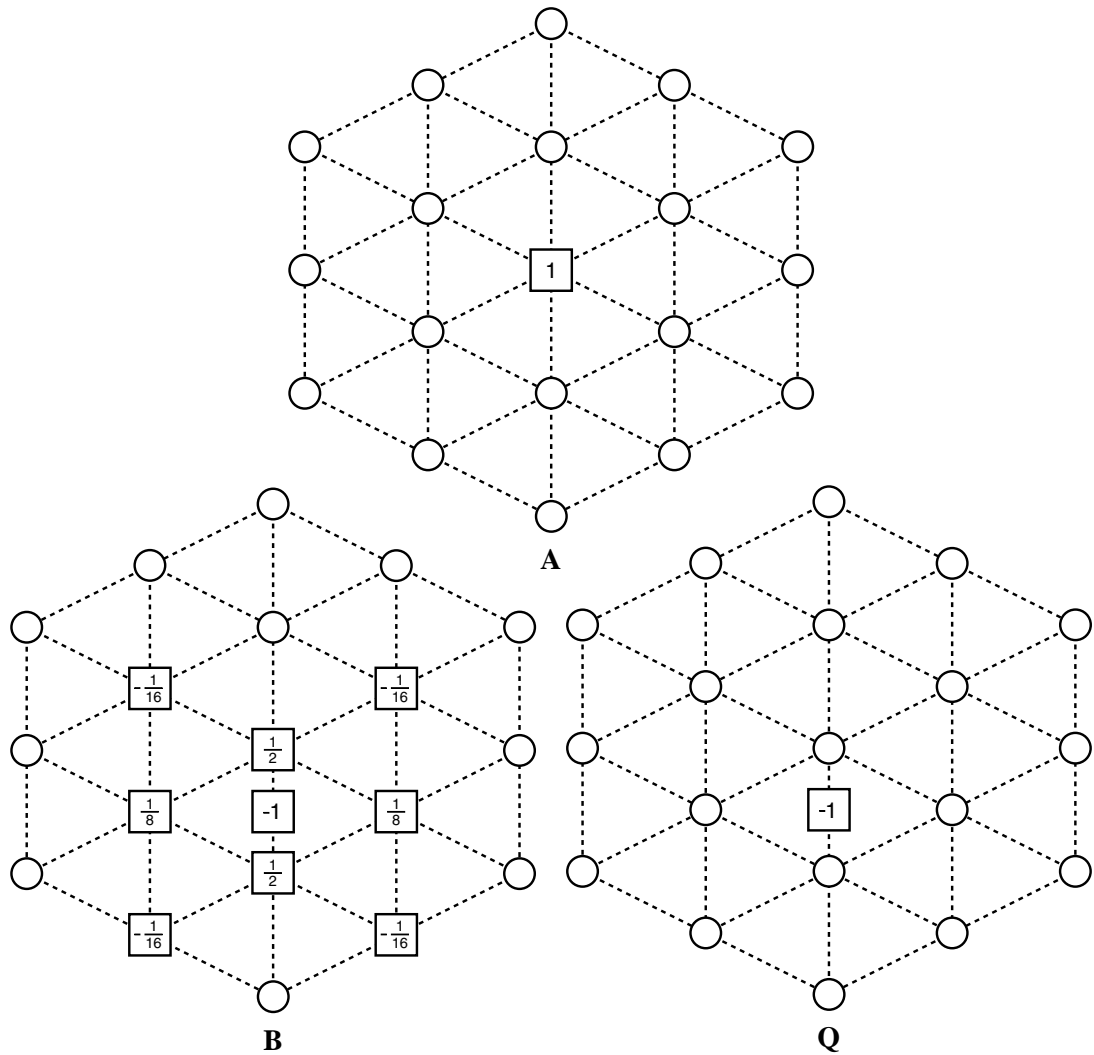


Figure 26: The Trivial Butterfly diagrams (**B** and **Q** in vertical-edge form)

Solving for the **A** diagrams of widths 1 and 2 for Butterfly subdivision produced no more than the trivial **A** diagram yet again. We may consequently regard the trivial **A** diagram as being the same as the **A** diagrams of widths 0, 1, and 2. The smallest nontrivial **A** diagram is of width 3. It is shown in Figure 27. The vertical-edge form of the **Q** diagram corresponding to this **A** and to the **B** diagram given in Figure 26 is shown in Figure 28. Wider diagrams have been found, but they will not be presented here.

It should be pointed out that the Butterfly multiresolutions we present here do not represent the first ones published for this subdivision. Apart from the trivial multiresolution, which must have been immediately obvious to Dyn, Levin, and Gregory, there are those of Schröder and Sweldens appearing in [8]. These latter multiresolutions, however, are constructed using lifting with respect to the classical, function-space norms, and consequently differ from the ones we are presenting.



but we consider only the regular, triangular case here. The **P** diagram for this subdivision on a regular, triangular mesh and a suitable **B** diagram is shown in Figure 29. As was the case for Butterfly and Loop

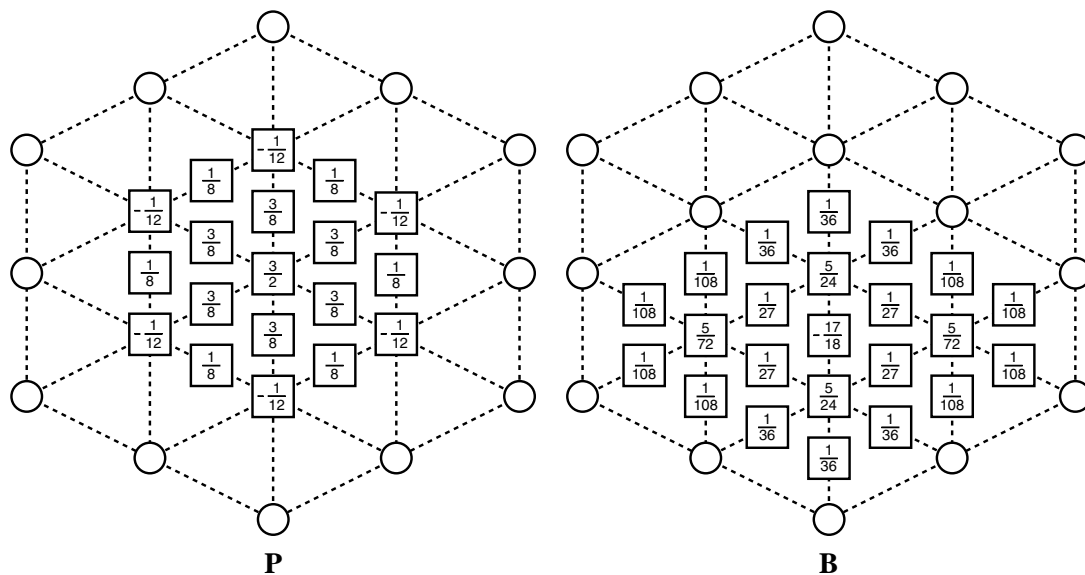


Figure 29: The **P** and (vertical form) **B** diagrams for regular Litke subdivision

subdivision, the **A** diagrams of width 1 and 2 for Litke subdivision prove to be the same. This minimal **A** diagram, together with its **Q** diagram is given in Figure 30 The next wider **A** diagram for regular Litke

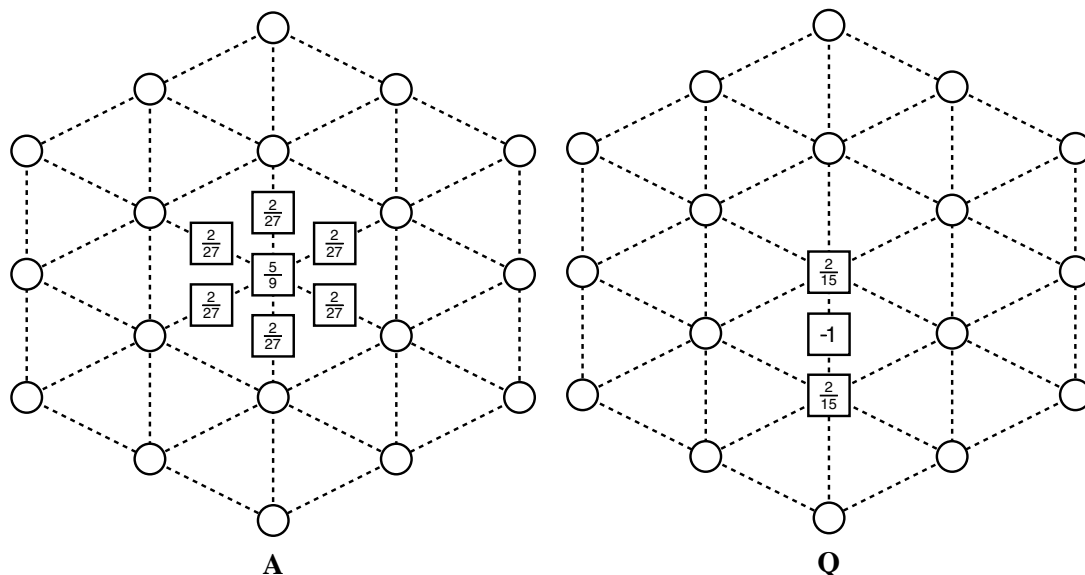


Figure 30: The Smallest Litke **A** and (vertical form) **Q** diagrams

subdivision has width 3. However, in comparison on sample data sets, this minimal width **A** proved to be comparable to the width-3 **A** of Butterfly subdivision in terms of the visual quality of the  $\mathbf{c}^k$  meshes produced and the size of the residuals  $\mathbf{P}\mathbf{c}^k - \mathbf{c}^{k+1}$  that are produced, so we shall be satisfied merely to show the multiresolution diagrams represented by Figures 29 and 30.

## 10 Surface Boundaries

In this section we present an example of the diagrammatic construction at and near the boundary of a regular triangular mesh. Butterfly subdivision will be used, since the rules on how to subdivide at the boundary are clearly stated in [12] and since the subdivision near the boundary is more involved than it would be in the subdivision of [6]. (The Butterfly subdivision mask has a larger footprint than the subdivision due to Litke, et. al., so points further from the boundary are affected by any special action that needs to be taken at the boundary.) The example will be given in just enough detail to permit the reader to carry it through to completion. This is done not only to conserve space, but also to provide a personal test to the reader that our presentation has been understood. If that is the case, the reader may then proceed to try out the construction in the neighborhood of special points, which are handled in a similar way.

According to [12], points along the natural boundary curve of a regular triangular mesh are to be subdivided using the curve version of Butterfly subdivision. It is important that subdivision at any point on the boundary be independent of any point in the interior of the mesh. This permits two surface meshes to be joined along a boundary curve, and independent subdivision of both meshes to the same level of fineness will not cause the joining boundary curves to separate. It is equally important, for the same reason, that our construction for estimating the  $\{c^k\}$  mesh boundary points from the  $\{c^{k+1}\}$  mesh also remain independent of interior points. Thus, the boundary multiresolution that we produce will separate into one that involves purely the boundary points, and one that involves the interior points near the boundary.

The interior points near the boundary are specified in [12] to be subdivided with reflection across the boundary. That is, if the normal mask that would be applied to generate a point of the fine mesh requires a point outside the existing mesh, that missing point is to be supplied by reflecting an appropriate interior point to the exterior location. In effect this redefines the coefficients of the affine combination and the mask in a band near the boundary.

The composite of the boundary subdivision and the near boundary subdivision yield the **P** diagrams shown in Figures 31 and 32. At any greater distance from the boundary, **P** is given by Figure 25.

The requirement that the boundary points not be influenced by interior mesh points results in the boundary **A** diagram shown in Figure 33. The trivial **B**, as in the interior, is simply the diagram that computes the residual at any edge point of  $\{c^{k+1}\}$ , and this is shown in Figure 34. Lastly, the equations  $\mathbf{A}\mathbf{Q} = \mathbf{0}$ ,  $\mathbf{B}\mathbf{Q} = \mathbf{I}$  can be solved numerically to yield the **Q** diagram shown in Figure 35.

Moving one level interior to the mesh boundary results in the **A** shown in Figure 36 where the values of the  $a_i$  are given in (10.1).

$$\begin{aligned}
 a_0 &= \frac{10994599}{16197945}, & a_1 &= \frac{695372}{16197945}, & a_2 &= \frac{558904}{16197945}, & a_3 &= \frac{4104824}{16197945}, \\
 a_4 &= \frac{4104824}{16197945}, & a_5 &= \frac{558904}{16197945}, & a_6 &= \frac{695372}{16197945}, & a_7 &= \frac{144937}{5399315}, \\
 a_8 &= -\frac{324096}{5399315}, & a_9 &= -\frac{6061}{1079863}, & a_{10} &= -\frac{171766}{5399315}, & a_{11} &= \frac{329297}{16197945}, \\
 a_{12} &= -\frac{4052398}{16197945}, & a_{13} &= \frac{329297}{16197945}, & a_{14} &= -\frac{171766}{5399315}, & a_{15} &= -\frac{6061}{1079863}, \\
 a_{16} &= -\frac{324096}{5399315}, & a_{17} &= \frac{144937}{5399315}, & a_{18} &= -\frac{369806}{5399315}, & a_{19} &= -\frac{360958}{16197945}, \\
 a_{20} &= \frac{360958}{16197945}, & a_{21} &= \frac{276916}{16197945}, & a_{22} &= -\frac{276916}{16197945}, & a_{23} &= \frac{267434}{16197945}, \\
 a_{24} &= \frac{9482}{16197945}, & a_{25} &= \frac{9482}{16197945}, & a_{26} &= \frac{267434}{16197945}, & a_{27} &= -\frac{276916}{16197945}, \\
 a_{28} &= \frac{276916}{16197945}, & a_{29} &= \frac{360958}{16197945}, & a_{30} &= -\frac{360958}{16197945}, & a_{31} &= \frac{360958}{16197945}, \\
 a_{32} &= \frac{360958}{16197945}
 \end{aligned} \tag{10.1}$$

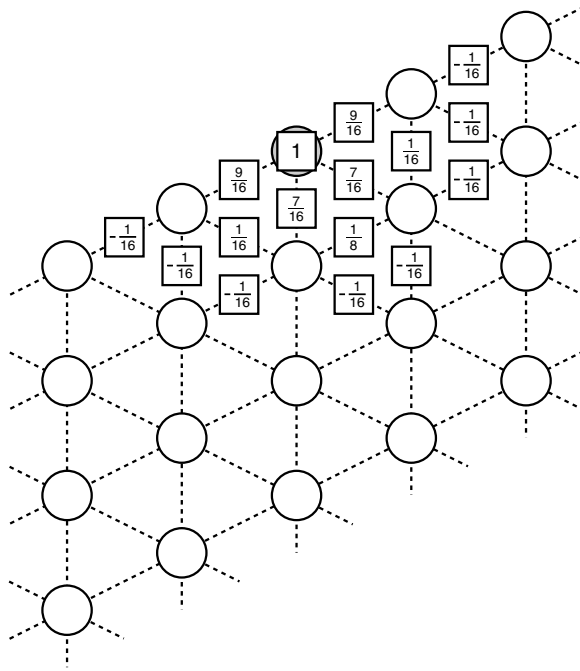


Figure 31: The  $\mathbf{P}$  diagram for Butterfly subdivision along the mesh boundary

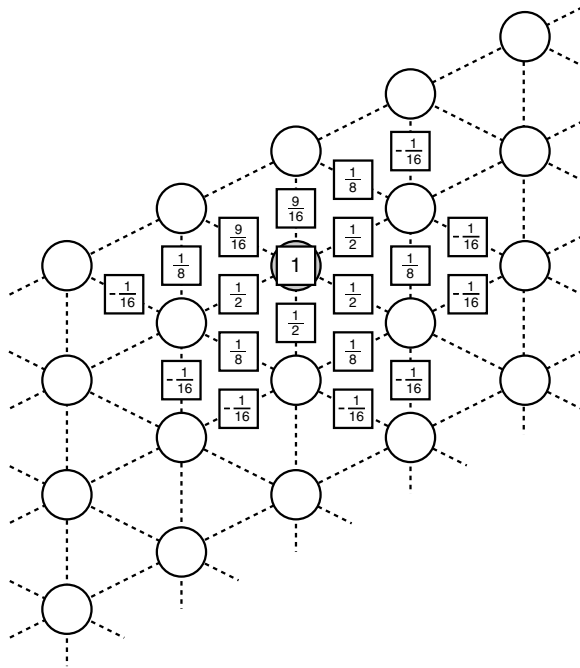


Figure 32: The  $\mathbf{P}$  diagram for Butterfly subdivision at points one level removed from the boundary

The reader is now invited to complete the discussion by generating a corresponding  $\mathbf{Q}$  from this  $\mathbf{A}$  and an appropriately oriented trivial  $\mathbf{B}$ . This exercise will need to be repeated at least one more level into the

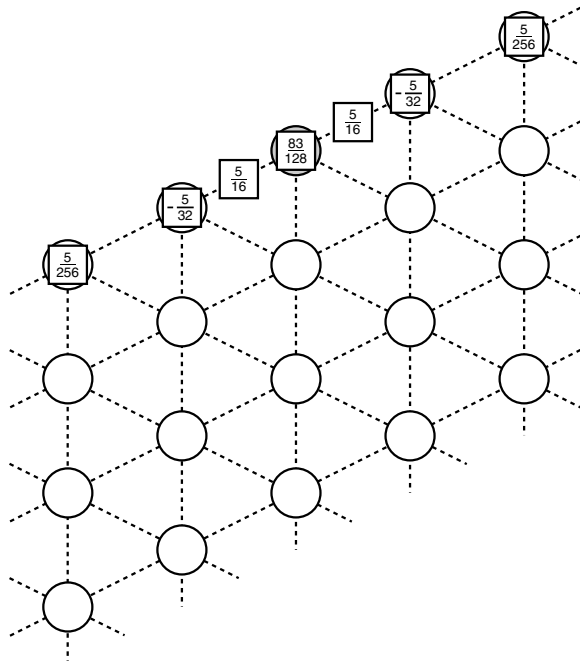


Figure 33: The Butterfly **A** diagram for points strictly on the boundary

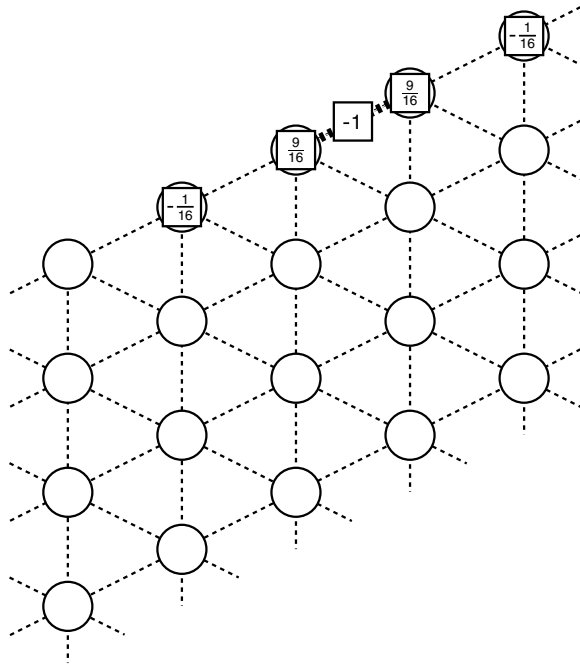


Figure 34: The Butterfly trivial **B** diagram for points strictly on the boundary

interior of the mesh before the effects of special subdivision rules at the boundary die away.

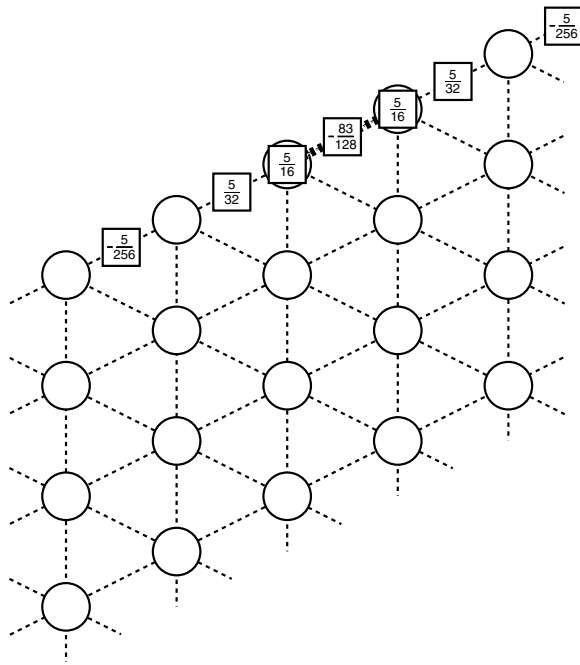


Figure 35: The Butterfly Q diagram for points strictly on the boundary

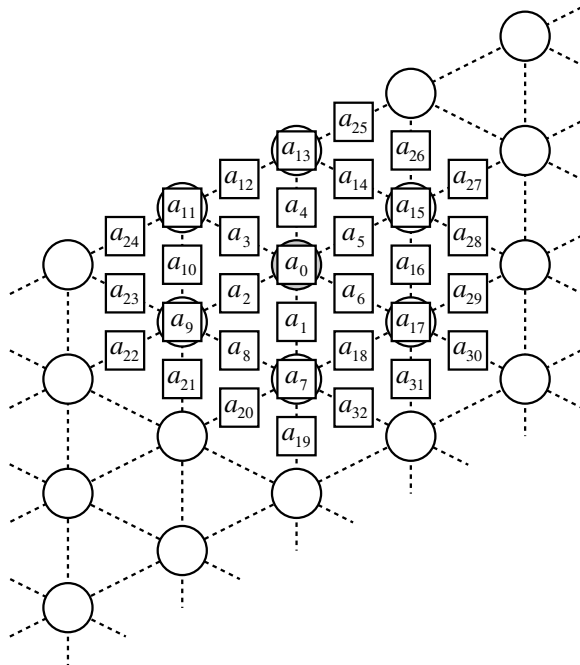


Figure 36: The Butterfly A diagram for points one level from the boundary

## 11 Examples

An example set of points  $\{c^{k+1}\}$  is provided by some commonly available range data for the U. S. Lincoln penny. We obtained our copy from the data sets provided with the Matlab system [5]. The data set is

arranged in rows and columns, but by omitting alternate points (even numbered points in even numbered columns and odd numbered points in odd numbered columns) we simulated a triangular mesh. We have, furthermore, extracted a central section of the data, since the margin of the penny data set provided by Matlab falls off abruptly.

Figure 37 shows the original Lincoln penny data  $\{c^{k+1}\}$ . Figure 38 shows the  $\{c^k\}$  points that are produced by the width-3 **A** diagram shown in Figure 27. Figure 39 shows the result of applying the width-3 **A** to the  $c^{k-1}$  points. Figure 40 shows the result of applying the width-3 **B** to the  $c^{k+1}$  points to obtain the detail information  $d^k$  that embodies the difference between subdividing the points  $c^k$  and the original data  $c^{k+1}$ . The usual observation that is made for wavelet-based multiresolutions holds here: the largest  $d^k$  are those that correspond to edges and high-profile features. Figure 41 is obtained by repeating the application of this **B** filter to the  $c^k$  points to produce the detail information  $d^{k-1}$ .

Figure 42 shows the exact reconstruction of the Lincoln  $c^{k+1}$  points from the  $c^{k-1}$ ,  $d^{k-1}$ , and  $d^k$  information obtained from the width-3 filters. Figure 43 shows the surface resulting from simply applying Butterfly subdivision twice to the  $c^{k-1}$  points; that is, it shows what happens if all  $d$  values are suppressed.

For multiresolution based upon Litke subdivision, all examples that we ran gave visual results from the width-1 **A** diagram and its cohorts comparable to those produced by the Butterfly multiresolution filters based upon the width-3 **A** diagram. Figures 44 through 48 show this.

## Acknowledgments

This work was carried out under funding by the Natural Sciences and Engineering Research Council of Canada and by NATO. The authors would like to thank Steve Mann for his helpful comments.

## References

- [1] R. H. Bartels and F. F. Samavati. Reversing subdivision rules: Local linear conditions and observations on inner products. *Journal of Computational and Applied Mathematics*, 119(1–2):29–67, July 2000.
- [2] N. Dyn, D. Levin, and J. Gregory. A 4-point interpolatory subdivision scheme for curve design. *Computer Aided Geometric Design*, 4(4):257–268, 1987.
- [3] Nira Dyn, David Levin, and John A. Gregory. A butterfly subdivision scheme for surface interpolation with tension control. *ACM Transactions on Graphics*, 9(2):160–169, April 1990.
- [4] K. M. Heal, M. L. Hansen, and K. M. Rickard. *Maple V Learning Guide*. Springer Verlag, 1996.
- [5] D. J. Higham and N. J. Higham. *The MATLAB Guide*. SIAM, 2000.
- [6] N. Litke, J. Levin, and P. Schröder. Trimming for subdivision surfaces. *Computer Aided Geometric Design*, 18(5):463–481, June 2001.
- [7] C. Loop. Smooth subdivision surfaces based on triangles. Master’s thesis, Department of Mathematics, University of Utah, 1987.

- [8] P. Schröder and W. Sweldens. Spherical wavelets: Efficiently representing functions on the sphere. In Robert Cook, editor, *SIGGRAPH 95 Conference Proceedings*, Annual Conference Series, pages 161–172. ACM SIGGRAPH, Addison Wesley, August 1995. held in Los Angeles, California, 06-11 August 1995.
- [9] E. H. Spanier. *Algebraic Topology*. McGraw-Hill, 1966.
- [10] W. Sweldens. The lifting scheme: A custom-design construction of biorthogonal wavelets. *Applied and Computational Harmonic Analysis*, 3(2):186–200, April 1996.
- [11] S. Wolfram. *The Mathematica Book, Fourth Edition*. Cambridge University Press, 1999.
- [12] D. Zorin, P. Schröder, and W. Sweldens. Interpolating subdivision for meshes with arbitrary topology. In Holly Rushmeier, editor, *SIGGRAPH '96 Conference Proceedings*, Annual Conference Series, pages 189–192. ACM SIGGRAPH, Addison Wesley, August 1996.

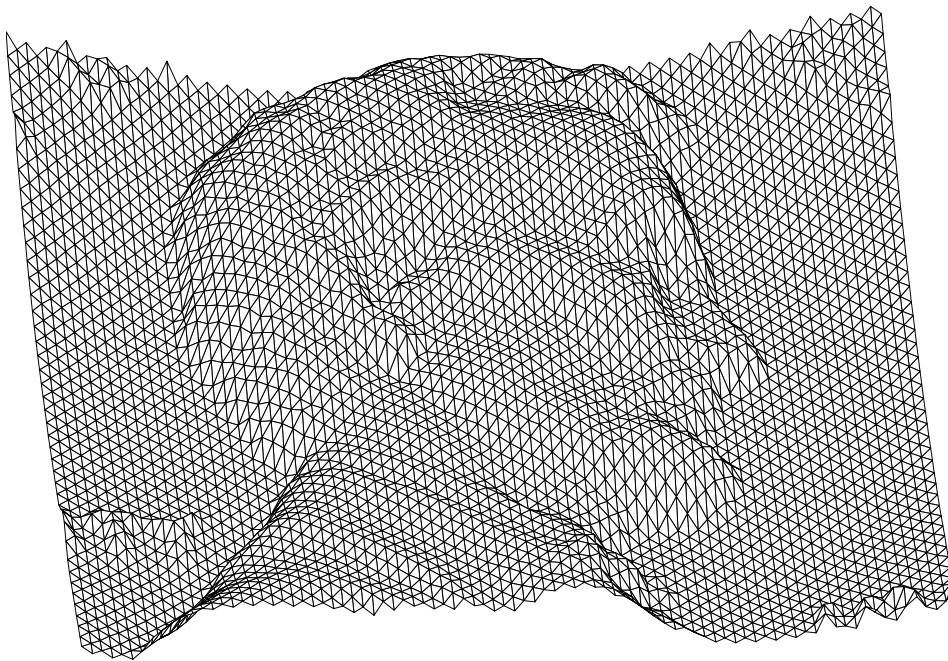


Figure 37: The Lincoln data set  $\{c^{k+1}\}$

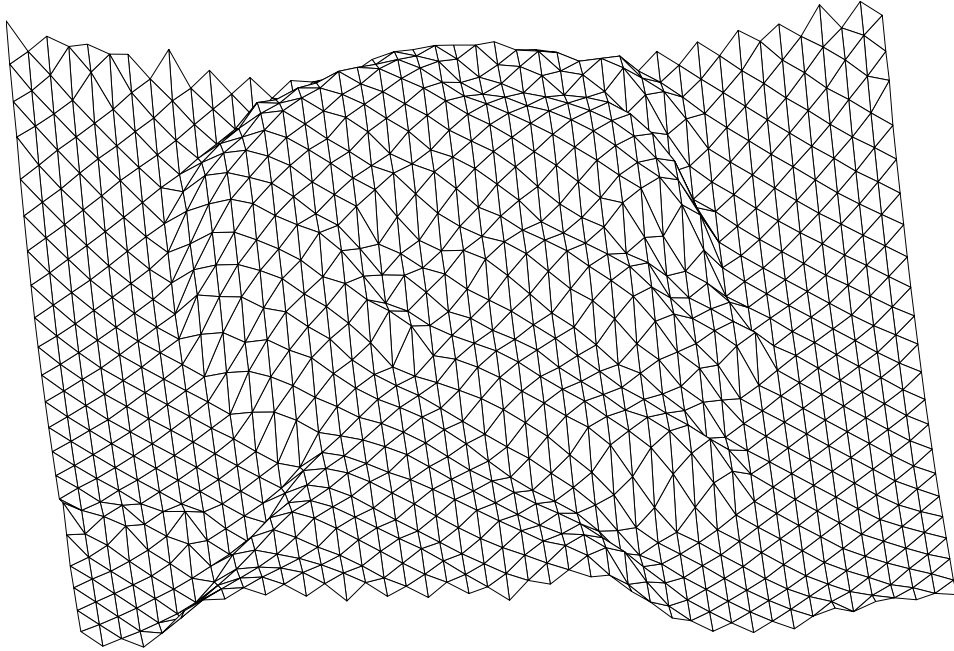


Figure 38: The Lincoln  $\{c^k\}$  points using the Butterfly width-3 **A**

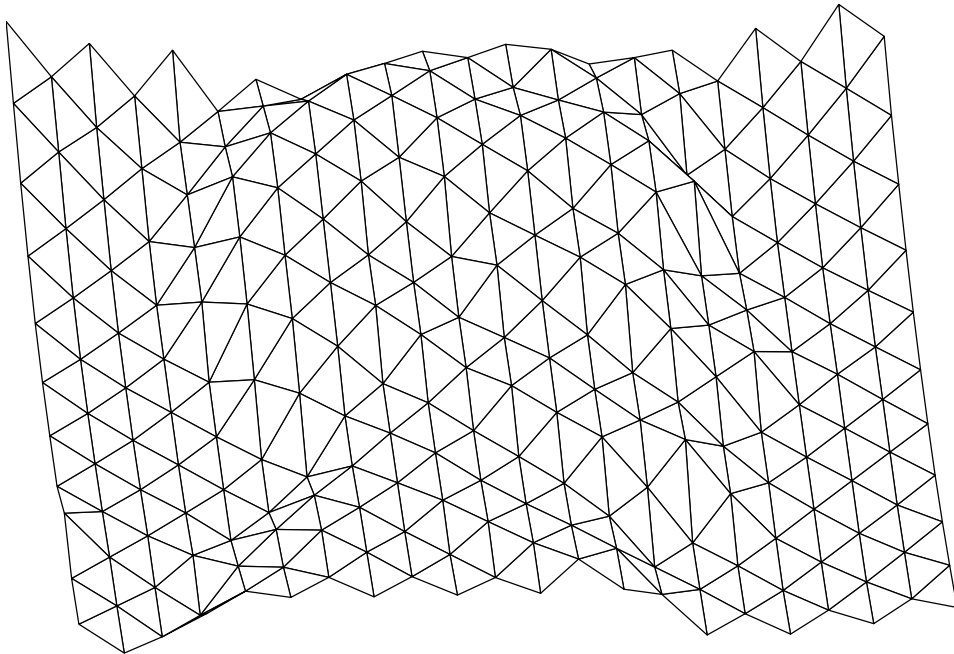


Figure 39: The Lincoln  $\{c^{k-1}\}$  points from a second application of the width-3 Butterfly **A**

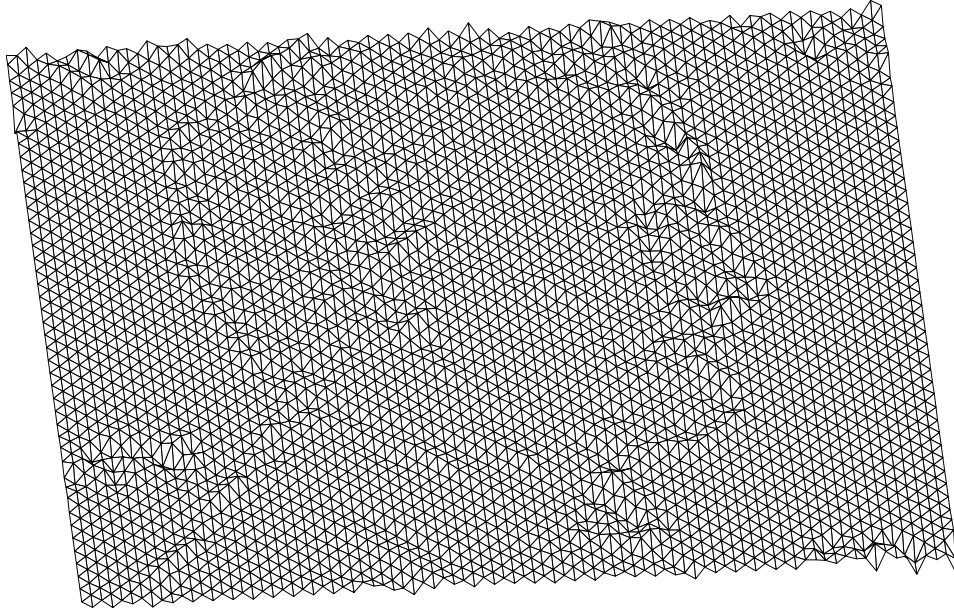


Figure 40: The Lincoln  $\{d^k\}$  information corresponding to the width-3 Butterfly **A**

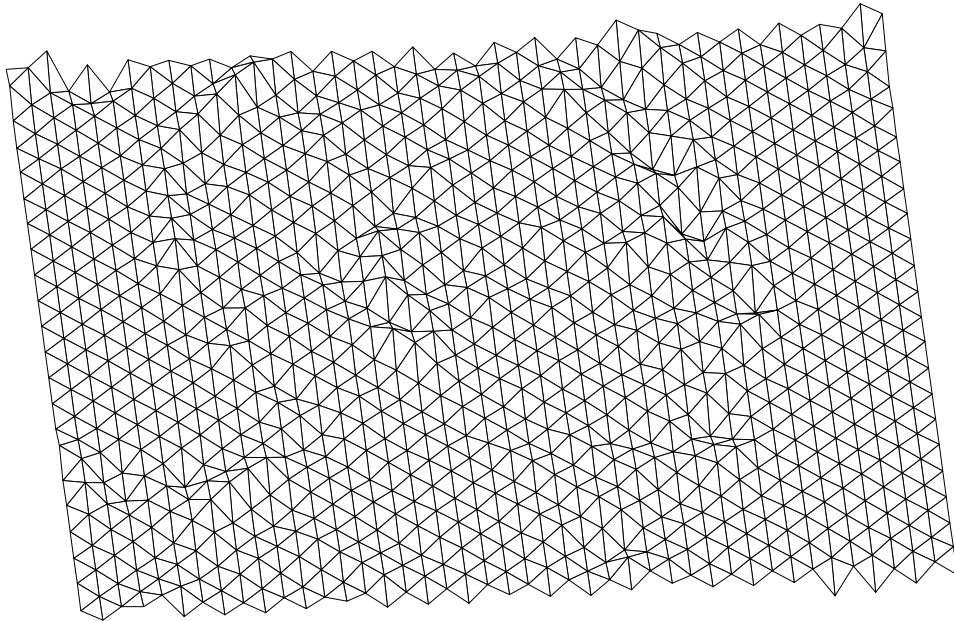


Figure 41: Lincoln  $\{d^{k-1}\}$  using the Butterfly **B** corresponding to the width-3 Butterfly **A**

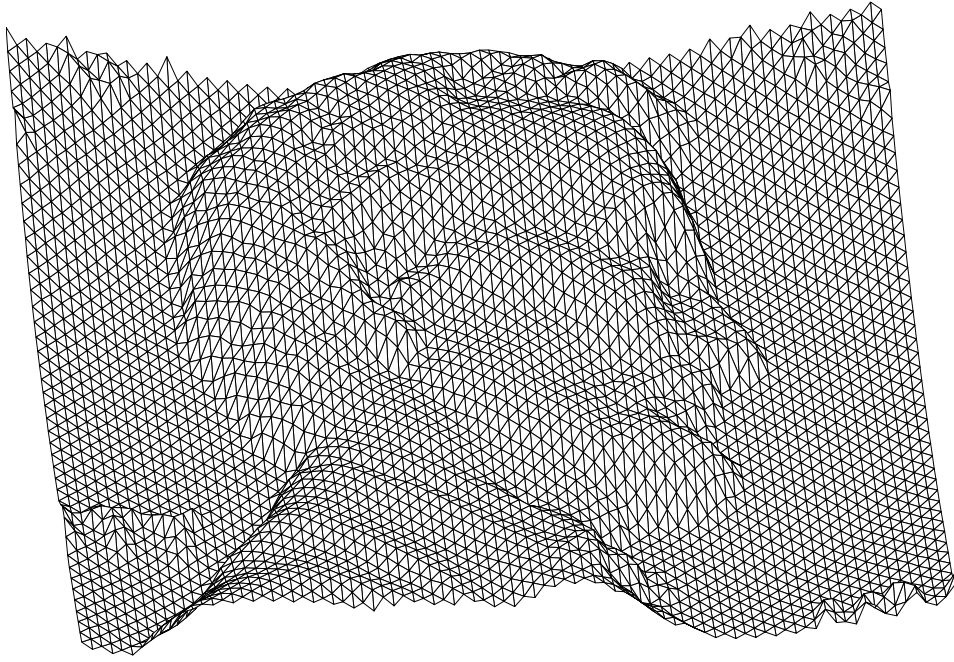


Figure 42: The Lincoln  $\{c^{k+1}\}$  data reconstructed from  $\{c^{k-1}\}$ ,  $\{d^{k-1}\}$ , and  $\{d^k\}$ , all corresponding to the width-3 Butterfly **A**

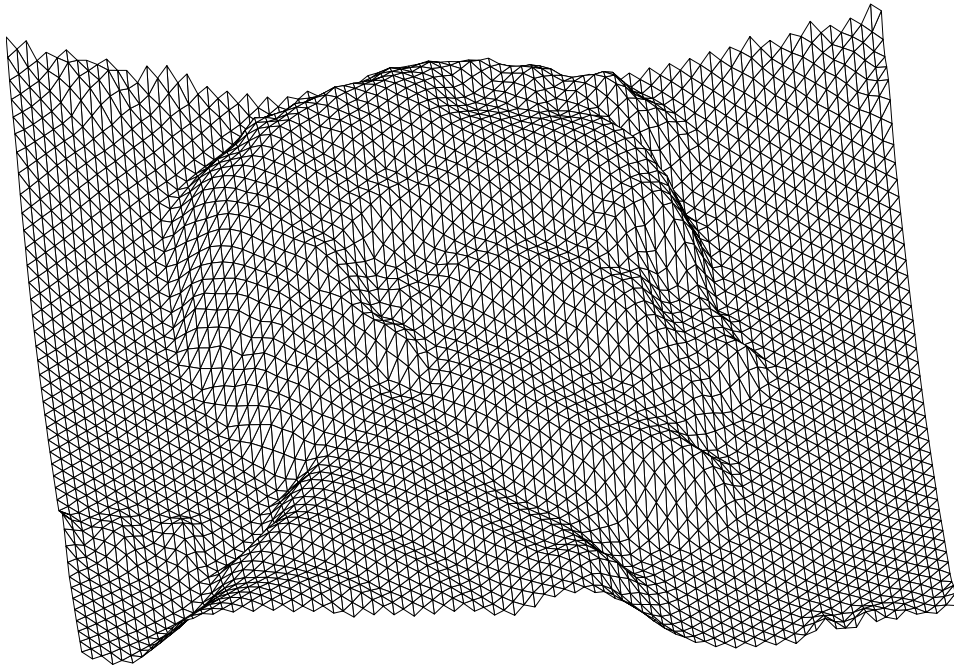


Figure 43: The Lincoln  $\{c^{k-1}\}$  data from the width-3 Butterfly **A**, subdivided twice (i.e. suppressing all  $d$ ), producing a subdivision surface  $\{s^{k+1}\}$

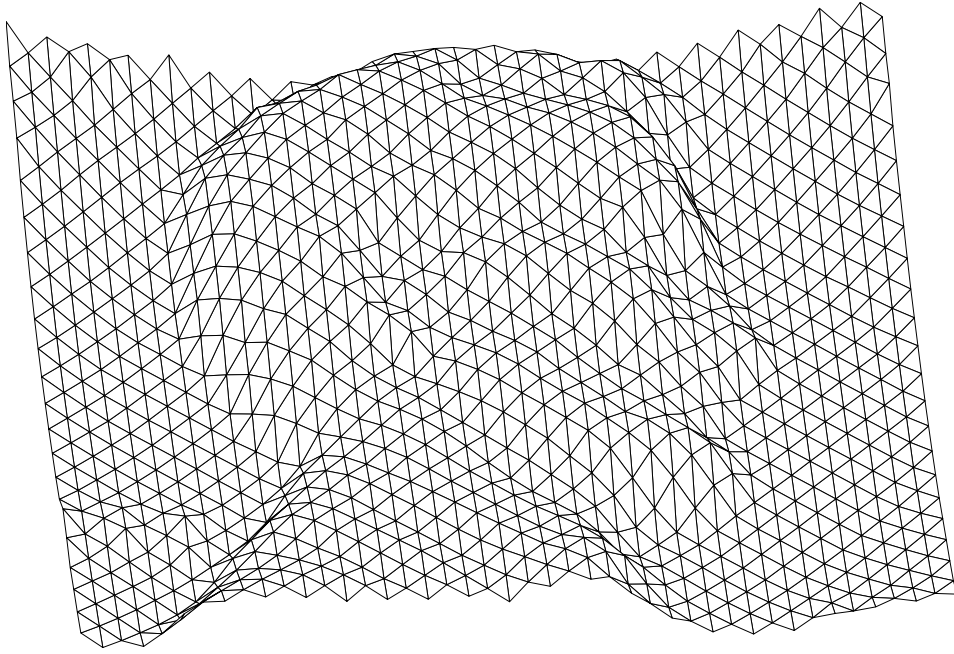


Figure 44: Lincoln  $\{c^k\}$  using Litke, width-1 **A**

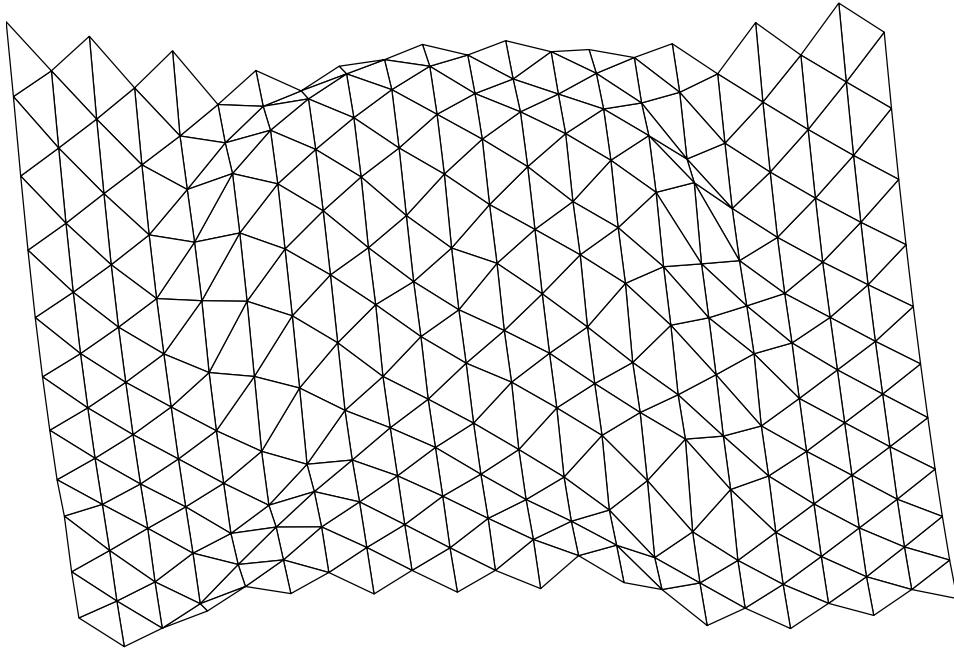


Figure 45: Lincoln  $\{c^{k-1}\}$  using Litke, width-1 **A**

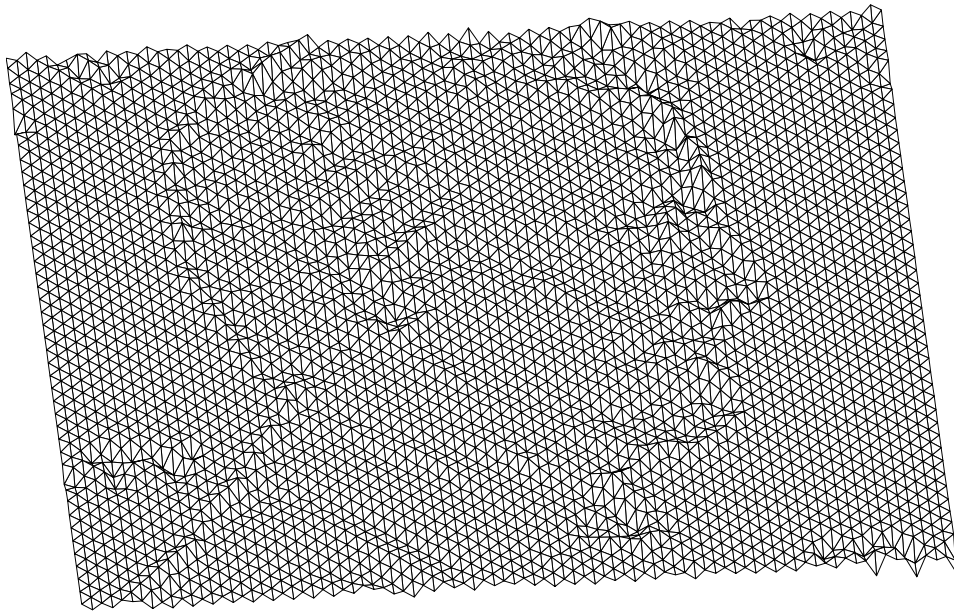


Figure 46: Lincoln  $\{d^k\}$  using Litke **B** for width-1 **A**

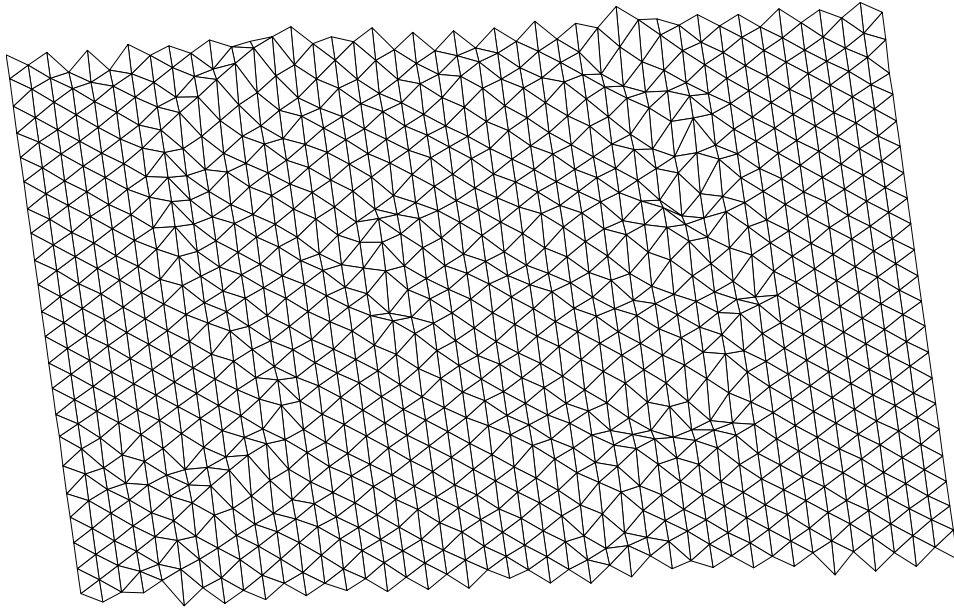


Figure 47: Lincoln  $\{d^{k-1}\}$  using Litke **B** for width-1 **A**

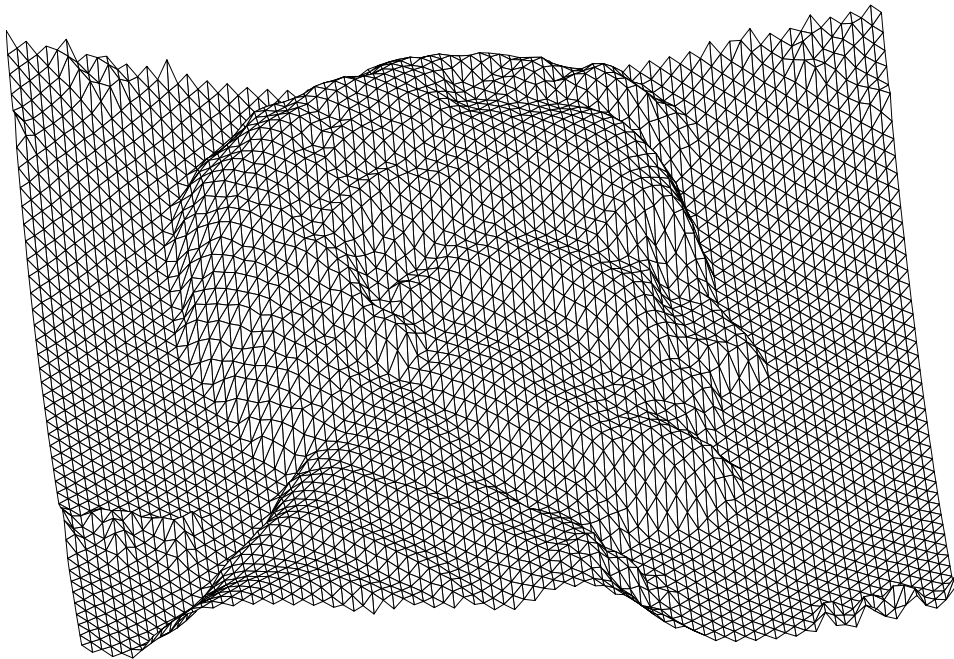


Figure 48: Lincoln reconstruction via Litke width-1 from  $\{c^{k-1}\}$ ,  $\{d^{k-1}\}$ , and  $\{d^k\}$